Investigations of Environmental Effects on Freeway Acoustics

Final Report 605-2
May 2013

Arizona Department of Transportation
Research Center

Investigations of Environmental Effects on Freeway Acoustics

Final Report 605-2
May 2013

Prepared by:
S. R. Shaffer
Center for Environmental Fluid Dynamics
Arizona State University
Tempe, AZ 85287-9809

H. J. S. Fernando
Center for Environmental Fluid Dynamics
Arizona State University
Tempe, AZ 85287-9809

N. C. Ovenden
Department of Mathematics
University College London
Gower Street, London WC1E 6BT, U.K.

Prepared for:
Arizona Department of Transportation
206 South 17th Avenue
Phoenix, AZ 85007
in cooperation with
U.S. Department of Transportation
Federal Highway Administration

This report was funded in part through grants from the Federal Highway Administration, U.S. Department of Transportation. The contents of this report reflect the views of the authors, who are responsible for the facts and the accuracy of the data, and for the use or adaptation of previously published material, presented herein. The contents do not necessarily reflect the official views or policies of the Arizona Department of Transportation or the Federal Highway U.S. Department of Transportation. This report does not constitute a standard, specification, or regulation. Trade or manufacturers' names that may appear herein are cited only because they are considered essential to the objectives of the report. The U.S. government and the State of Arizona do not endorse products or manufacturers.

Technical Report Documentation Page

1. Report No.	2. Government Accession No.	3. Recipient's Catalog No.
FHWA-AZ-13-605-2		

4. Title and Subtitle	5. Report Date
Investigations of Environmental Effects on Freeway Acoustics (original: Environmental Measurements in support of traffic generated noise)	May 2013
	6. Performing Organization Code

7. Author	8. Performing Organization Report No.
S. Shaffer (Center for Environmental Fluid Dynamics, Arizona State University) H.J.S. Fernando (Center for Environmental Fluid Dynamics, Arizona State University) N. Ovenden (Department of Mathematics, University College, London)	

9. Performing Organization Name and Address	10. Work Unit No.
Arizona State University Office for Research & Sponsored Projects Administration P.O. Box 873503 Tempe, AZ 85287-3503	
	11. Contract or Grant No. SPR 000-1(169) 605-2

12. Sponsoring Agency Name and Address	13. Type of Report & Period Covered
Arizona Department of Transportation 206 S. 17th Avenue Phoenix, Arizona 85007	Final Report 01/01/2009 to 12/31/2010
	14. Sponsoring Agency Code

15. Supplementary Notes

16. Abstract

We present a generalized terrain PE (GTPE) model for sound propagation in non-uniform terrain following the work of Sack and West (1995). Results for simplified terrain cases illustrate the new model's capabilities and the effects of terrain in a neutral atmosphere. The model is extended by deriving a reflection scheme to account for two-way propagation. Thus, our model enables the study of backscatter from vertical terrain features and forward propagation of traffic noise in complex terrain. Future developments will extend the reflection scheme to terrain features with arbitrary angles. Future possibilities include coupling the sound model with flow calculation software to determine the flow response to terrain and the sound field response to perturbed flow.

Additionally, we apply ARW-WRF v3.2's new option of vertical nesting within the finest nest to a numerical experiment studying highway noise pollution in the Phoenix metropolitan area. This experiment was conducted for comparison on November 7, 2006, in Phoenix by Ovenden et al (2009). Vertical profiles with near-ground resolution finer than 20 m were extracted for input into a sound propagation model to produce forecasts of noise pollution from a highway line segment noise source. Vertical nesting improved the resolution of finer structures in the temperature and velocity profiles. Ovenden et al. (2009) previously demonstrated sensitivity of the resultant sound field within 600 m of the source to input effective sound speed vertical profiles, $C_{eff}(z)$, in the lowest 300 m of the planetary boundary layer. Hence, resolution of such features is important when forecasting $C_{eff}(z)$ for use in the highway noise propagation model.

17. Key Words	18. Distribution Statement	23. Registrant's Seal
Noise propagation, meteorological effects, acoustic modeling, field studies, noise exposure, mitigation strategies, freeway noise, Weather Research and Forecasting model, Noise Forecasting	Document is available to the U.S. public through the National Technical Information Service, Springfield, Virginia 22161	

19. Security Classification	20. Security Classification	21. No. of Pages	22. Price
Unclassified	Unclassified	73	

SI* (MODERN METRIC) CONVERSION FACTORS

APPROXIMATE CONVERSIONS TO SI UNITS

Symbol	When You Know	Multiply By	To Find	Symbol
		LENGTH		
in	inches	25.4	millimeters	mm
ft	feet	0.305	meters	m
yd	yards	0.914	meters	m
mi	miles	1.61	kilometers	km
		AREA		
in^2	square inches	645.2	square millimeters	mm^2
ft^2	square feet	0.093	square meters	m^2
yd^2	square yard	0.836	square meters	m^2
ac	acres	0.405	hectares	ha
mi^2	square miles	2.59	square kilometers	km^2
		VOLUME		
fl oz	fluid ounces	29.57	milliliters	mL
gal	gallons	3.785	liters	L
ft^3	cubic feet	0.028	cubic meters	m^3
yd^3	cubic yards	0.765	cubic meters	m^3
		NOTE: volumes greater than 1000 L shall be shown in m^3		
		MASS		
oz	ounces	28.35	grams	g
lb	pounds	0.454	kilograms	kg
T	short tons (2000 lb)	0.907	megagrams (or "metric ton")	Mg (or "t")
		TEMPERATURE (exact degrees)		
^oF	Fahrenheit	5 (F-32)/9 or (F-32)/1.8	Celsius	^oC
		ILLUMINATION		
fc	foot-candles	10.76	lux	lx
fl	foot-Lamberts	3.426	$candela/m^2$	cd/m^2
		FORCE and PRESSURE or STRESS		
lbf	poundforce	4.45	newtons	N
lbf/in^2	poundforce per square inch	6.89	kilopascals	kPa

APPROXIMATE CONVERSIONS FROM SI UNITS

Symbol	When You Know	Multiply By	To Find	Symbol
		LENGTH		
mm	millimeters	0.039	inches	in
m	meters	3.28	feet	ft
m	meters	1.09	yards	yd
km	kilometers	0.621	miles	mi
		AREA		
mm^2	square millimeters	0.0016	square inches	in^2
m^2	square meters	10.764	square feet	ft^2
m^2	square meters	1.195	square yards	yd^2
ha	hectares	2.47	acres	ac
km^2	square kilometers	0.386	square miles	mi^2
		VOLUME		
mL	milliliters	0.034	fluid ounces	fl oz
L	liters	0.264	gallons	gal
m^3	cubic meters	35.314	cubic feet	ft^3
m^3	cubic meters	1.307	cubic yards	yd^3
		MASS		
g	grams	0.035	ounces	oz
kg	kilograms	2.202	pounds	lb
Mg (or "t")	megagrams (or "metric ton")	1.103	short tons (2000 lb)	T
		TEMPERATURE (exact degrees)		
^oC	Celsius	1.8C+32	Fahrenheit	^oF
		ILLUMINATION		
lx	lux	0.0929	foot-candles	fc
cd/m^2	$candela/m^2$	0.2919	foot-Lamberts	fl
		FORCE and PRESSURE or STRESS		
N	newtons	0.225	poundforce	lbf
kPa	kilopascals	0.145	poundforce per square inch	lbf/in^2

*SI is the symbol for the International System of Units. Appropriate rounding should be made to comply with Section 4 of ASTM E380.
(Revised March 2003)

CONTENTS

LIST OF FIGURES

LIST OF TABLES

LIST OF ABBREVIATIONS AND ACRONYMS

1D	one dimensional
2D	two dimensional
AGL	above ground level
ARW-WRF v3.2	Advanced Research Weather-Weather Research Forecasting version 3.2
C_{eff}	effective sound speed
C_{eff} *(z)*	effective sound speed vertical profiles
CISL	Computational and Information Systems Laboratory
dB	decibel
dBA	decibels, A-weighted
GTPE	generalized terrain parabolic equation
Hz	hertz
kHz	kilo hertz
NCAR	National Center for Atmospheric Research
PBL	planetary boundary layer
PE	parabolic equation
RDA	Research Data Archive
RRTM	rapid radiative transfer model
SPL	sound pressure level
UTC	universal standard time
WRF	weather research and forecasting
YSU	Yonsei University (South Korea)

ACKNOWLEDGMENTS

This work was supported by the Arizona Department of Transportation (ADOT). We are extremely grateful to ADOT, Arizona State University (ASU), and University College London (UCL) for their support of this ongoing collaborative research. In particular, we thank Christ Dimitroplos at ADOT for his continued interest and support. The data for weather research and forecasting (WRF) initialization in this study are from the Research Data Archive (RDA), which is maintained by the Computational and Information Systems Laboratory (CISL) at the National Center for Atmospheric Research (NCAR). NCAR is sponsored by the National Science Foundation (NSF). The original data are available from the RDA (http://rda.ucar.edu) in dataset number ds083.2. We also acknowledge the support of the staff at ASU High-Performance Computing Center for maintaining the Saguaro cluster.

EXECUTIVE SUMMARY

The modeling system for evaluating environmental effects on freeway acoustics, presented in ADOT SPR 605-1, is advanced in three important areas, namely, (i) the inclusion of terrain, (ii) accounting for acoustic backscatter from vertical terrain features using a new technique, and (iii) the use of a regional weather model to produce limited area forecasts for input into the highway noise propagation model. These developments overcome the previous limitations of considering only the flat terrain, while further enabling the inclusion of noise walls in a physically realistic manner, as well as incorporating simulated meteorological profiles for studies where observed profiles may be insufficient or lacking. The new modeling system has been applied to several test cases, allowing model validation by comparing with data. Recommendations for further improvements and applications of this modeling suite are also given.

KEY RESULTS

- A numerical implementation of smooth terrain profiles to a two-dimensional parabolic equation sound propagation model was accomplished, with the starting acoustic perturbation profile obtained via coupling with a Green's function solution for line-sources transverse to the plane of propagation.
- A numerical implementation of a technique to determine the reflected acoustic field due to vertical terrain features was conducted, utilizing the normal-impedance boundary condition and parameterizing material properties via acoustic impedance.
- The influence of terrain on the acoustic field of a single line-source in a medium with a constant sound speed was identified for several benchmark cases.
- A demonstration of the influence on acoustic propagation of a vertical wall placed atop an escarpment terrain is presented highlighting both the changes in sound pressure level beyond the wall as well as details of the sound waves reflected off the wall that propagate back across a symmetric escarpment highway canyon.
- A method for forecasting profiles of effective sound speed as inputs to a flat-terrain, two-dimensional parabolic equation model was proposed based on a nested mesoscale meteorological modeling system. The generated wind predictions were compared to actual field measurements, along with an intercomparison between the resultant acoustic model predictions using simulated versus observed sound speed profiles.
- A technique is presented for refining the vertical resolution of the meteorological model, which could be used to derive profiles of effective sound speed by capturing near-ground temperature inversions and wind shear, thus improving the resultant acoustic model forecast.

RECOMMENDATIONS

Regarding the inclusion of terrain:

- Further model evaluations should be performed, including benchmark comparisons and calculations of sound wave diffraction around simple terrain features. Some literature resources are given.
- As-built freeway plans along with regulations on design limitations should be consulted for devising more realistic terrain configuration cases.
- Computational fluid dynamics software such as FLUENT could be used to generate simulated meteorological fields for cases of noise propagation in urban areas with built elements.
- Laboratory and field testing should consider aspects that would provide sufficient evaluation of numerical implementation for complex flow situations over canyon/wall/facades of varying geometries and material properties. Furthermore, optimal placement of microphones for sound measurements could be well informed by modeling.
- Careful evaluations should be carried out for the calculations of backscattered field from terrain with arbitrary angles and for barriers with facades tilted slightly from vertical.

Regarding the noise forecasting model:

- Sensitivity of the computed acoustic field to the variations in model input profiles of effective sound speed should be examined, to determine the necessary degree of accuracy for input profiles.
- Meteorological model evaluation should explore sensitivity of derived effective sound speed profiles to the selection of physical parameterizations of the model (e.g. planetary boundary layer, surface layer and land surface and land use models).
- Issues regarding forecast timing, phase-errors, and magnitudes (e.g. wind gust or front passage timing and direction), need to be explored, particularly for regions such as the Phoenix metropolitan area with typical diurnal flows largely due to local topographic forcing.
- Methods for nesting eddy-resolving simulations could be considered for merging mesoscale meteorological profiles with idealized microscale terrain influences. This may open new avenues of investigation for incorporating turbulence effects into acoustic propagation models.

I. INTRODUCTION

The urban soundscape is influenced by many factors, including the bustle of daily human activities. Among the set of anthropogenic sources are crowded areas, such as stadiums or busy sidewalks; passing airplanes and trains; and, most commonly, motor vehicle traffic. Highway noise pollution has been associated with adverse effects in areas ranging from human health (Moudon 2009; Passchier-Vermeer and Passchier 2000) and housing prices (Nelson 1982) in populated urban and suburban settings to wildlife in more remote areas (Rheindt 2003; Forman and Deblinger 2000). It is of interest to city planners to account for noise, defined as undesired sound, when designing transportation systems and to consider noise mitigation in areas that are already receiving complaints of traffic noise or are in violation of the Federal Highway Administration (FHWA) Noise Abatement Criterion. (Areas are in violation of the FHWA criterion when noise levels exceed 67 dBA; here A-weighting is used to represent human sensitivity to hearing by applying a band-pass-filter.) Regarding traffic noise, existing mitigation strategies, such as constructing sound walls or utilizing rubberized asphalt, are quite expensive. Thus the efficacy of their placement for mitigation purposes must be carefully considered.

Motivated by complaints from residents of Scottsdale about noise from the ever-expanding Loop 101, where some typical noise mitigating measures had already been implemented, the Arizona Department of Transportation (ADOT) began collaboration with Arizona State University and other partners to improve understanding of highway noise pollution and mitigation methods. This project was initiated as a part of the Quiet Pavement Pilot Program. The focus of our earlier work (Ovenden et al. 2009) was to understand the fundamental role of meteorology in the propagation of sound from freeway corridors. We developed a parabolic equation (PE) model capable of incorporating single meteorological profiles of temperature and crosswind velocity (as effective sound speed) above a flat impedance plane. We concluded that under conditions of temperature inversion and/or low-level wind shear, areas up to 600 m from the roadway (treated as a single coherent effective line source) were in violation of the FHWA criterion and thus would require further mitigation. We also found that frequencies around 0.8 to 1 kHz were most influenced by this atmospheric refraction effect.

The work reported here focuses on extending the previous model by introducing additional parameters typical of real highway settings. In so doing, the first simplification we remove is related to terrain, where a terrain-following coordinate transformation in the original Helmholtz equation was used to account for the topography. We present a new, generalized terrain parabolic equation (GTPE) model following the work of Sack and West (1995) (see Chapter II of this report). Simplified terrain cases without meteorological effects to illustrate the capabilities of the new model evaluating different terrains in a neutral atmosphere. Our discussion centers on plans for future enhancements, including treating the effective sound speed derived from meteorology as a 2D scalar field instead of a 1D profile. This would enable us to model flow response to terrain along with turbulence and not just mean flow. At present, the GTPE model has been extended by deriving a reflection scheme based on the normal impedance ground boundary condition to account for two-way propagation. Thus our new model enables the study of backscatter from vertical terrain features and deals with the

forward propagation of traffic noise in settings with complex terrain. Future model developments will extend the reflection scheme to terrain features with arbitrary angles.

We further extend modeling capabilities by testing the possibility of coupling the PE sound model with a meteorological model. We apply the new option of vertical nesting implemented in the weather research and forecasting (WRF) model, ARW-WRF v3.2, to the finest nest of a numerical experiment, for studying highway noise pollution in the Phoenix metropolitan area. Vertical profiles with near-ground resolution finer than 20 m are extracted from a calculation and input into the PE sound propagation model to produce forecasts of noise pollution from a highway line segment noise source. We demonstrate that vertical nesting improves the resolution of finer structures in the temperature and velocity profiles, such as morning temperature inversions and low-level, jet-like features.

The previous study by Ovenden et al. (2009) (also known as OSF09 and as ADOT 605-1 2010) demonstrated the sensitivity of the sound field within 600 m of the source in order to input effective sound speed vertical profiles, $C_{eff}(z)$, in the lowest 300 m of the planetary boundary layer. Hence, resolution of such meteorological features is important when forecasting $C_{eff}(z)$ for use in the highway noise propagation model. We use the field experiments from Ovenden et al. (2009) on November 7, 2006, in Phoenix as a reference for comparison.

This study extends the previous work in several important and distinct ways. The first, discussed in Chapter II, extends the ground boundary from a flat boundary to a terrain-following boundary while accounting for acoustic reflections from vertical terrain features. The second, presented in Chapter III, explores the possibility of using the WRF model to forecast the near-ground meteorological profiles needed to calculate the effective sound speed for input into the acoustic model. Future work exploring a means of coupling the work in Chapters II and III is outlined in Chapter IV, followed by recommendations and conclusions in Chapter V.

II. GENERAL TERRAIN PARABOLIC EQUATION MODEL

This chapter will discuss our application and extension of the GTPE model of Sack and West (1995). The organization of this chapter is as follows:

- An introduction to and motivation for this study are briefly discussed in §II.A.
- The GTPE and reflection model is presented in §II.B, with the terrain-following transformation and boundary condition given in §II.B.1.
- A derivation of our vertical terrain backscatter approximation is given in §II.B.2.
- We then present several model validation and application experiments to demonstrate the model capabilities in §II.C.
- A discussion and conclusions follow in §II.D, with future directions proposed in §II.E.

II.A. INTRODUCTION

Traditionally, the applications of PE modeling are one-way calculations, often with flat or piecewise linear terrain using a rotated coordinate system. However, notably absent in the context of highway noise is any accounting for backscatter from terrain features. We have derived a simple method for calculating the back-reflected field using the normal impedance boundary condition and the first-order PE approximation and changing variables to a terrain-following vertical coordinate. Using the reflected component in a reverse running calculation and iterating over several subsequent back reflections, a more representative prediction of the effects (such as reverberation) of terrain features of various impedances and geometries on the 2D sound field can be made. Furthermore, the relevant meteorological parameters of temperature and flow velocity can be incorporated into the model by treating the effective sound speed as a 2D scalar field obtained by prediction with numerical techniques or extrapolation from field experiment measurements. The sound field can then be assessed under the influence of varying terrain boundary conditions, as can the subsequent coupling through feedback on the meteorological field due to the terrain modifications which in turn will influence the sound field by the way of a modified refractive index scalar field.

II.B. GTPE AND REFLECTION MODEL

We follow Sack and West's (1995) method for the GTPE model and apply it to a Gaussian hill, an escarpment with and without a wall, and a symmetric canyon, treating the reflection from a theoretical wall on top of the escarpment. In general, it is best to determine the back-reflected field at all points in the range, but a first approximation can be made by considering only the reflection from vertical boundaries (such as a barrier or wall). This approximation can then be enhanced to account for boundaries tilted slightly from vertical and for general terrain boundaries. In this report, we show results only for reflection from vertical barriers.

II.B.1. Terrain-Following Coordinates and Boundary Conditions

The *(x,z)* Cartesian coordinate system, with *z* vertical and *x* in the direction of propagation, can be transformed into terrain-following coordinates quite simply by changing the variables *ξ=x* and *η=z-H(x)*, where the terrain height above some reference point is given by the function *H(x)*. The core of our method is to apply the normal impedance boundary condition of Sack and West (1995) (their Equation 24),

$$\partial_{\vec{n}}\,\psi = \frac{\partial \psi}{\partial \vec{n}} = -ik_0\hat{\beta}\psi\,, \qquad \text{(Eq. 1)}$$

for an appropriate representation of the normal derivative $\partial_{\vec{n}}$. The ground normal vector, $\vec{n}$, is always away from the ground, $\hat{\beta} = \rho_0 c Z^{-1}$, is an admittance defined in terms of a reference fluid density ρ_0, characteristic sound speed *c,* and representative complex ground impedance value *Z.* We chose a simple two-parameter model for the ground impedance which depends on the frequency of interest and an effective flow resistivity representative of the acoustic interaction with a porous material (Attenborough et al. 2007; Delany and Bazley 1970; Ovenden et al. 2009). The complex velocity potential $\psi = \varphi\,\exp(ik_0\xi)$ is written in terms of a complex modulator φ multiplied by an exponential carrier term with reference wavenumber k_0 and transformed horizontal coordinate ξ.

In general, the outward normal derivative $\partial_{\vec{n}}$ to a slope at an angle δ from vertical is defined in transformed coordinates by

$$\partial_{\vec{n}} = -(\sin\delta)^{-1}\partial_\eta - \cos\delta\,\partial_\xi\,. \qquad \text{(Eq. 2)}$$

II.B.2 Vertical Terrain Backscatter Approximation

We begin with the simplest case for a vertical wall and set $\delta = 0$ at the position of the wall, $\xi = \xi_w$, so Equation 2 now reads

$$\partial_{\vec{n}} = -\partial_\xi\,. \qquad \text{(Eq. 3)}$$

We now write the total field as the sum of the left and right traveling components, using an over-arrow to distinguish, as $\psi = \overleftarrow{\psi} + \vec{\psi}$. Upon substitution of Equation 3 into Equation 1, we have

$$\partial_\xi\left(\overleftarrow{\psi} + \vec{\psi}\right) = ik_0\rho_0 c Z_w^{-1}\left(\overleftarrow{\psi} + \vec{\psi}\right) \quad \text{at} \quad \xi = \xi_w, \qquad \text{(Eq. 4)}$$

as the boundary condition for the total field on the face of a vertical obstacle with surface impedance Z_w. Next, the wavenumber for the left and right traveling components are written as $\overleftarrow{k_0} = -k_0$ and $\overrightarrow{k_0} = k_0$, respectively. Separating the left from the right components, we arrive at

$$\left[ik_0\rho_0 cZ_w^{-1} + ik_{0w} - \partial_\xi\right]\overleftarrow{\psi} = \exp(2ik_{0w}\xi_w)\left[\partial_\xi + ik_{0w} - ik_0\rho_0 cZ_w^{-1}\right]\vec{\psi}\,, \qquad \text{(Eq. 5)}$$

where k_{0w} is the wavenumber at the face of the wall. The next key step of our method uses Equations 10–12 from Sack and West (1995) for the first-order or narrow angle PE operator. Written here in the notation of the left-traveling component as

$$\partial_\xi \overleftarrow{\varphi} = \frac{-i}{2k_0}\overleftarrow{L}_1[\overleftarrow{\varphi}]\,. \qquad \text{(Eq. 6)}$$

where the left traveling first order (narrow angle) PE operator $\overleftarrow{L}_1$, is defined in general (without direction) as

$$L_1[\varphi] = (1 + (H')^2)\partial_{\eta\eta}\varphi - (H'' - 2ik_0H')\partial_\eta\varphi + k_{0w}^2 - k_0^2\,. \qquad \text{(Eq. 7)}$$

For a vertical wall, we take H' and H'' both equal to 0. We thus obtain the approximation

$$\overleftarrow{L}_1^{(v)}[\overleftarrow{\varphi}] \approx \partial_{\eta\eta}\overleftarrow{\varphi} + k_{0w}^2 - k_0^2\,, \qquad \text{(Eq. 8)}$$

where the superscript (*v*) is used to denote the L_1 operator for the vertical terrain case.

II.C. GTPE MODEL TEST CASES

The general domain configuration used in these test cases was a 300 m high by 300 m in-range grid with 10 points per wavelength. The only case with a different range was the symmetric canyon, which was the same as for the escarpment with barrier and symmetric about the origin, except it did not extend beyond the barriers. For all but the reflected field case in §II.C.4, a road section of width 6.7 m using the one parameter ground impedance model of Delany and Bazley (1970) was used with a flow resistivity representative of asphalt σ = 3 x 10^7 Pa s m^{-2} (Attenborough 2007). This was used in conjunction with a Green's function solution for an infinite line source above an impedance plane to obtain the starting complex pressure field at the edge of the road in a manner identical to Ovenden et al. (2009). For the remainder of the domain, the ground flow resistivity value was changed to 4 x 10^5 Pa s m^{-2}, which is a value representative of hard sandy soil. The flow resistivity model variable can be vectorized to vary with range, but the creation of artificial diffraction at impedance discontinuities within the PE model has yet to be explored. The terrain function was also constrained to vary smoothly after the edge of the road to avoid artificial diffraction. In all cases, an attenuating layer was placed at the top third of the PE model domain to eliminate numerically reflected waves. The source heights and frequencies are described for each case.

II.C.1. Gaussian Hill

Due to the smoothness constraints, which were imposed to minimize artificial diffraction at terrain discontinuities when the function is discretized onto the computational grid, we chose

to use a Gaussian profile rather than the sine-squared profile used in Sack and West (1995). We also scaled down the domain size significantly, but the results are qualitatively similar.

II.C.1.1. Model and Domain Setup

The terrain function used for this case is

$$H(x) = 40e^{-((x-206)/50)^2} \text{ m}, \qquad \text{(Eq. 9)}$$

giving a hill of 50 m half-width centered at 206 m in range (~200 m from the edge of the pavement) with a height of 40 m. The source height was placed at 5 m above ground level (AGL) with a source strength of S = 1 so that since $\log_{10}(1) = 0$, the output dB field would then show attenuation with respect to the source. However, there is a shift in the results shown by -20 dB in the terrain case and +52 dB in the flat comparison (which can be revised as appropriate). The meteorological fields were held constant, giving a neutral atmosphere, with T = 25°C and U = 0 m s^{-1} (meters per second). This case was run for a set of 17 frequency bands, displayed in Figure 1. The output from the first nine bands is presented in Appendix D, and the 63 Hz band is shown in this section.

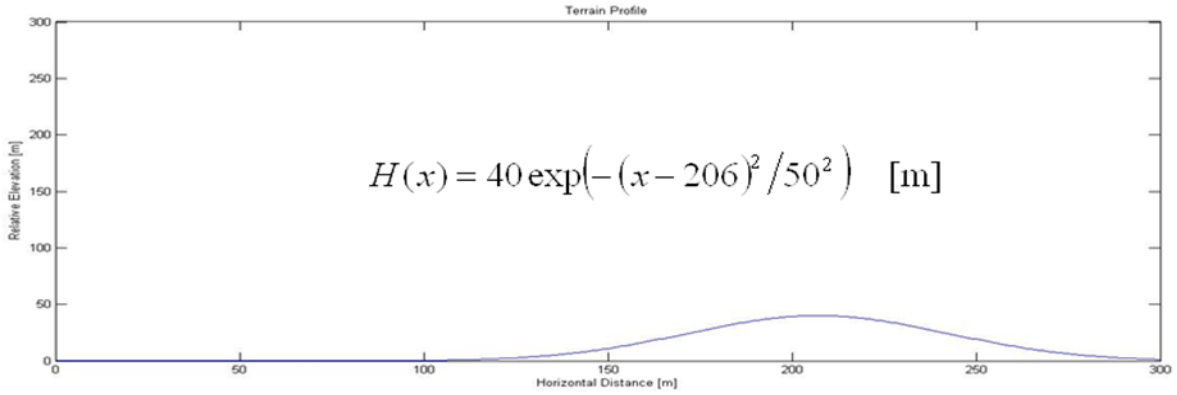

Figure 1. GTPE Case: Gaussian Hill Configuration.

The terrain profile used for the Gaussian Hill Case (Figure 1) along with parameters of the setup configuration is shown above. The set of frequencies for which output was created are also given.

II.C.1.2. Model Results

Figures 2 and 3 show the cases for flat terrain and Gaussian hill, respectively. In Figure 3, the terrain-following transformation has been inverted for illustration. The black region at the top is above the computational grid, and the brown region at the bottom represents the ground below the computational grid. Regions of white contours are below the minimum contour level. The attenuating layer is most visible above 250 m, and contours above 200 m are therefore diminished. Note that high angles in both the PE and GTPE models lose accuracy. Also note the region of constructive and destructive interference on the near side of the hill, the diffraction pattern from the top of the hill and down range, and the acoustic shadow region down range. Figure 4 (top) is a zoom in the lowest 60 m, showing the detail of the sound field near the terrain. Figure 4 (bottom) shows an attenuation versus range plot at 2 m AGL, comparing sound levels in the range against the level at 50 m from the source (see §III.B.5, Equation 16). Figure 5 shows results for 7 of the 17 frequency bands computed, showing how each frequency responds to the terrain. Since the model is to be extended to account for meteorological profiles, we did not pursue the aspect of nondimensionalization, which would be difficult to define in any useful way for any but the neutral case.

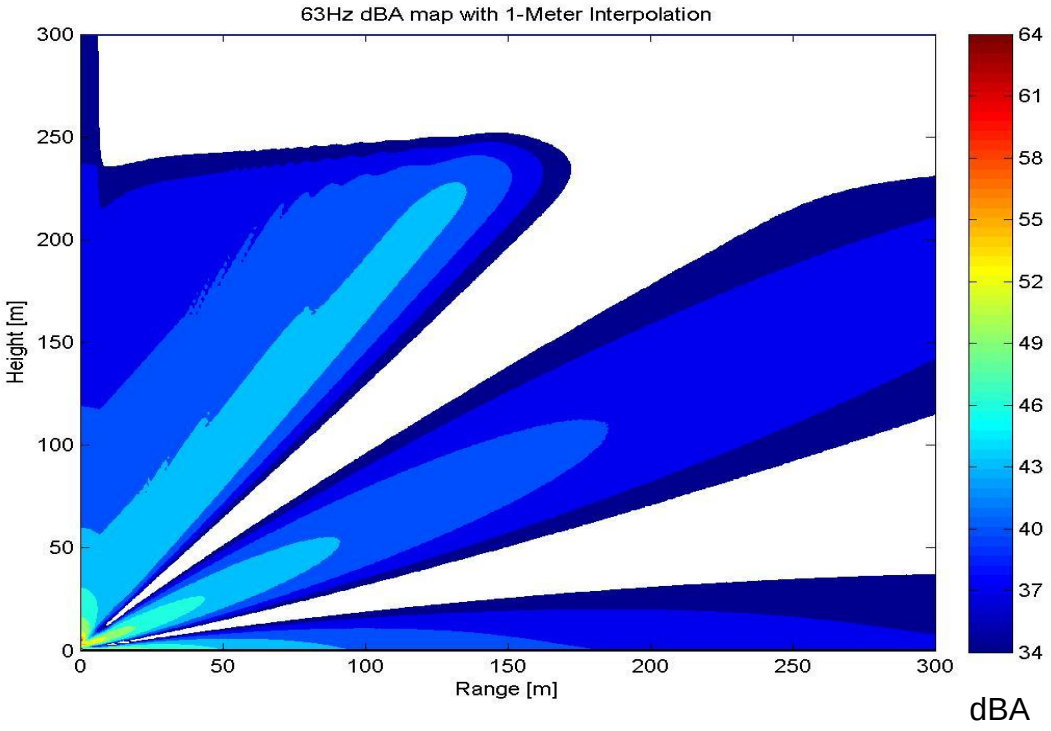

Figure 2. Flat Terrain Comparison for 63 Hz, T=25°C, and U=0 m s^{-1} for the Entire Domain.

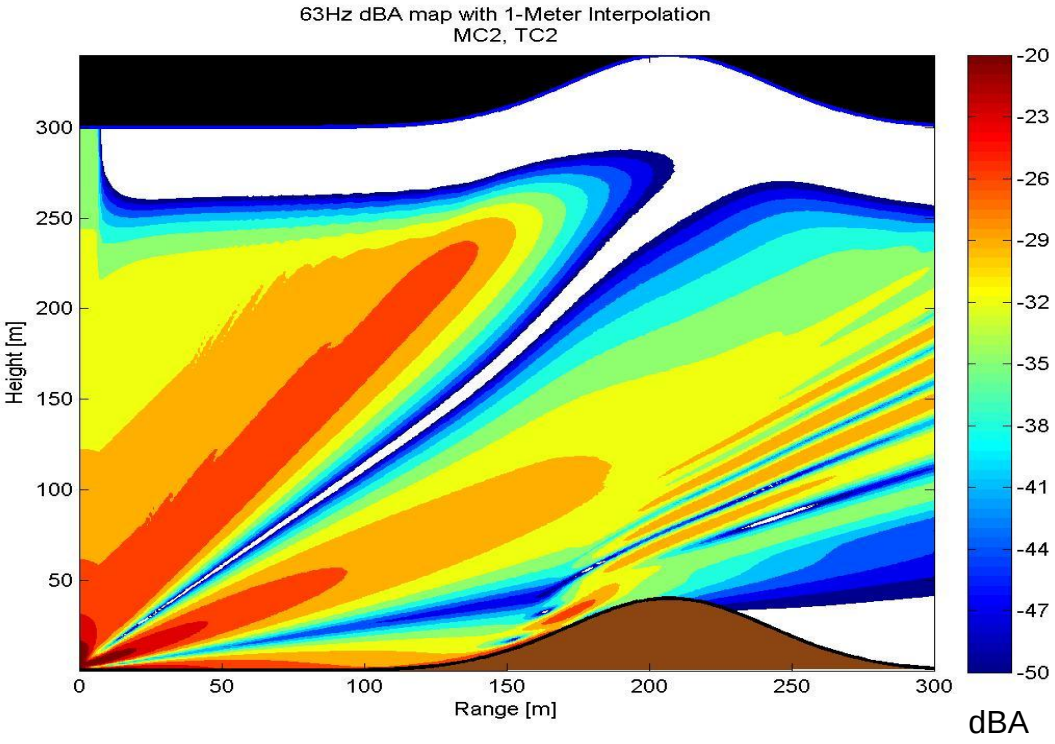

Figure 3. GTPE Case: Gaussian Hill.

Results shown are for 63 Hz, T=25°C, and U=0 m s^{-1} for the entire domain.

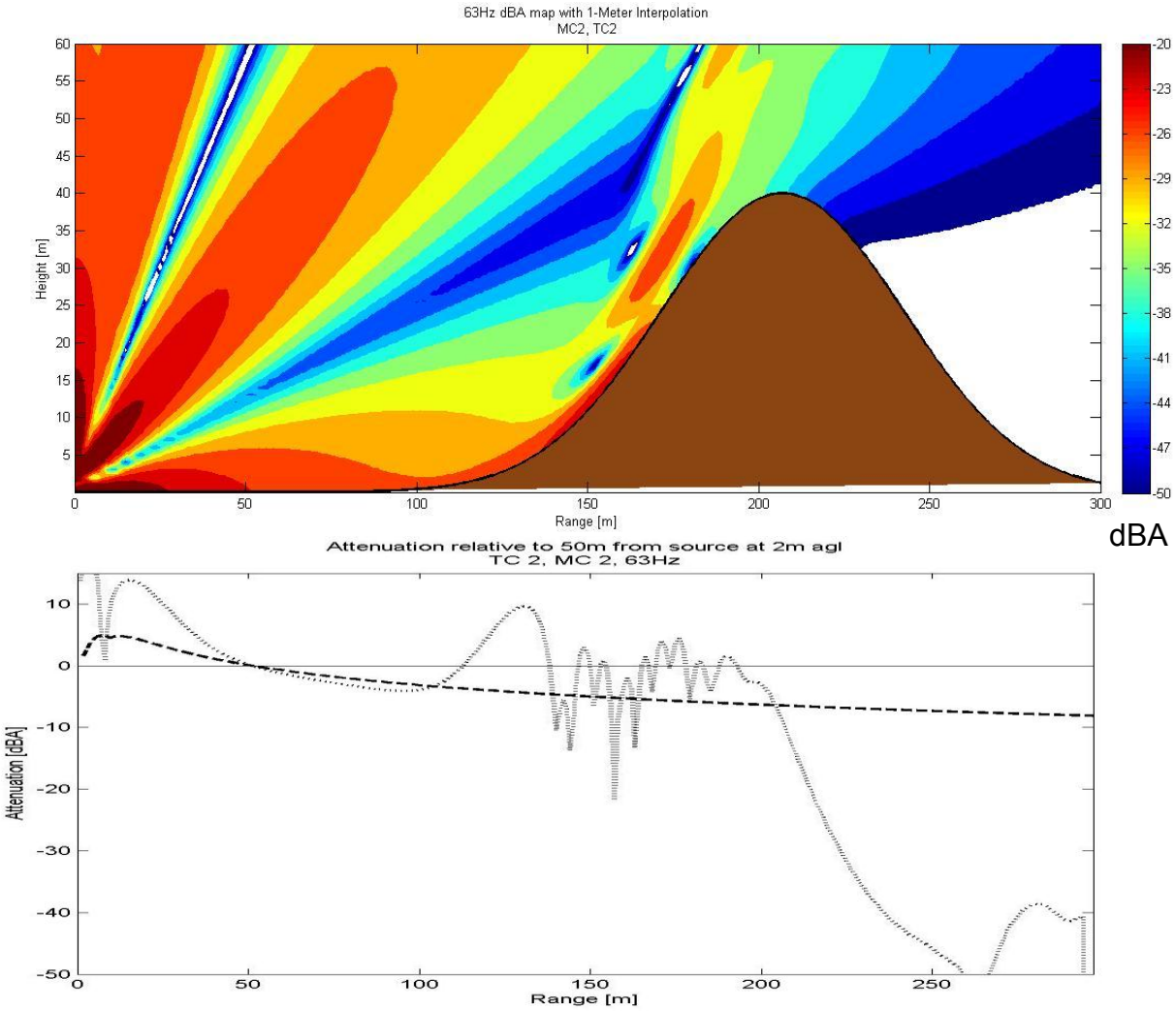

Figure 4. GTPE Case: Gaussian Hill Zoom.

Gaussian hill results for 63 Hz zoomed to the lowest 60 m (top) and attenuation versus range at 2 m AGL (bottom) for the flat comparison (dashed) and with terrain (dotted).

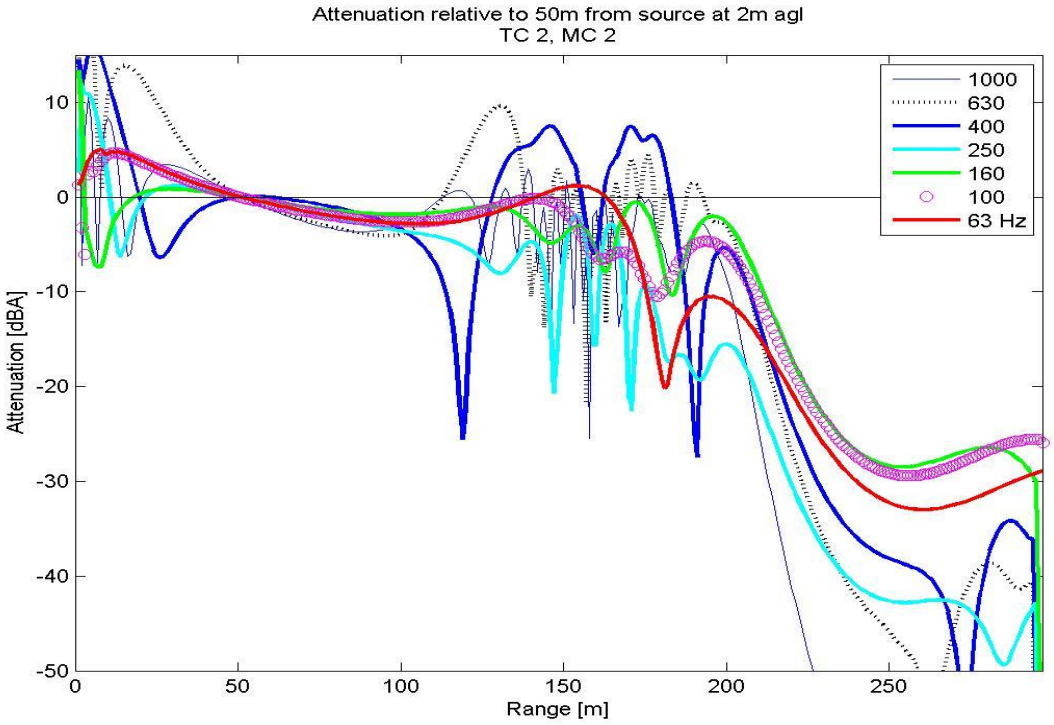

Figure 5. GTPE Case: Gaussian Hill Range Plot.

II.C.1.3. Comparison to Literature Benchmarks

For comparison with the Gaussian hill, we present the results from Sack and West (1995). The terrain function used in their work is

$$H(x) = \begin{cases} a\cos^2\left[\frac{\pi x_{top}}{W}\left(1 - \frac{x}{x_{top}}\right)\right], & \frac{W}{2} \le x \le W = 1\text{ km} \\ 0, \quad \text{elsewhere} \end{cases}, \qquad \text{(Eq. 10)}$$

where the hill height a = 200 m, the width W = 1 km, and the center x_{top} = 1 km. They use a 50 Hz source at 2 m height with U = 0 and T = constant. Reproduced here in Figure 6 is Figure 7 from their work, showing the resultant sound field for this case. A comparison of the qualitative features with those in Figure 3 indicates good agreement.

Figure 7—a reproduction of Figure 6 from Sack and West (1995)—shows attenuation at 2 m AGL relative to 100 m from the source for geometric attenuation (solid smooth line), GTPE results for their terrain case (solid irregular line), and results obtained using Maekawa barrier diffraction approximation (dashed line).

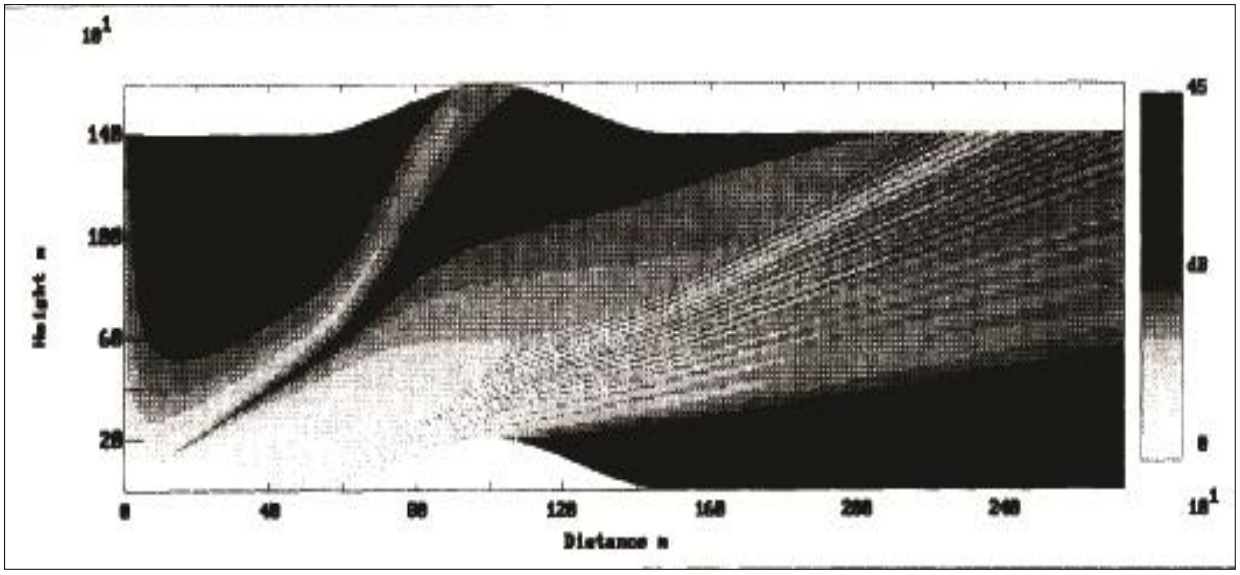

Figure 6. Comparison Figure Sound Field.
(Reprinted from Applied Acoustics 45 (2), Sack and West, "A Parabolic Equation for Sound Propagation in Two Dimensions Over Any Smooth Terrain Profile: The Generalized Terrain Parabolic Equation (GT-PE)," pages 113-129, fig. 7, © 1995, with permission from Elsevier.)

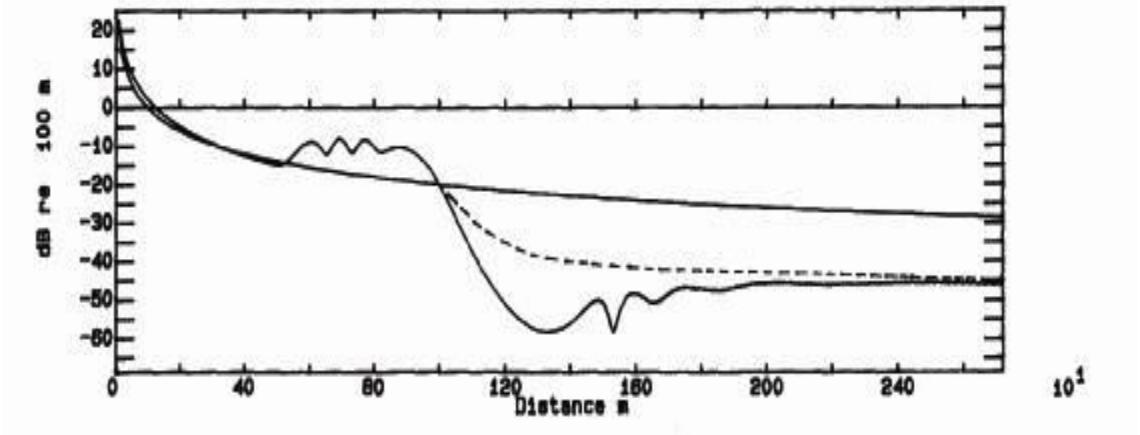

Figure 7. Comparison Figure Range Plot.
(Reprinted from Sack and West, fig. 6, (1995) with permission from Elsevier.)

II.C.2. Escarpment

To explore a terrain configuration similar to a highway canyon, a smooth escarpment was chosen. Note that we still use a scale very different from the actual cases to show the general effect of including terrain.

II.C.2.1. Model and Domain Setup

The terrain function used in this case is

$$H(x) = .5\,A\,\left(\tanh\left(\frac{x-x_c}{W}\right)+1\right), \qquad \text{(Eq. 11)}$$

where A = 10 m scales the height of the escarpment, x_c = 30 + 7 m shifts the center of the feature by 30 m and accounts for the Green's function domain of 6.7 m (and rounding up), and the slope angle is controlled by varying W, which is set to 20 m in this case. The other model parameters are identical to the case outlined in §II.C.1.1, namely U = 0 m s^{-1}, T = 25°C, and S = 1 and height = 1 m.

II.C.2.2. Model Results

The PE starter field is computed with a Green's function solution initialized at 6.7 m from the line source with a ground porosity representative of asphalt transitioning to hard sandy soil in the PE domain (σ=3x10^7 and 4x10^5 Pa s m^{-2}). The escarpment is defined by Equation 11. The dimensions of the escarpment were chosen to be quite large to demonstrate the effects of terrain as a first step. A larger set of values will be tested in the future.

Shown in Figure 8 are the contours representing the attenuation from the source, shown in increments of -3dB normalized on the basis of the PE starting field. As in Figure 3, regions outside the computational domain are shaded black (above) and brown (below), and white regions represent values below the minimum contour level. Similar to results from §II.C.1, the diffraction pattern from the slope, along with the constructive and destructive interference patterns on the near side, are quite evident. Also present is an acoustic shadow region on top of the escarpment. Contour levels of -3dB are the attenuation one expects from geometrical spreading of a line source when doubling distance in a neutral atmosphere. The Green's function starting field is present out to 6.7 m, and the exponentially attenuating layer above 200 m is evident beyond 6.7 m.

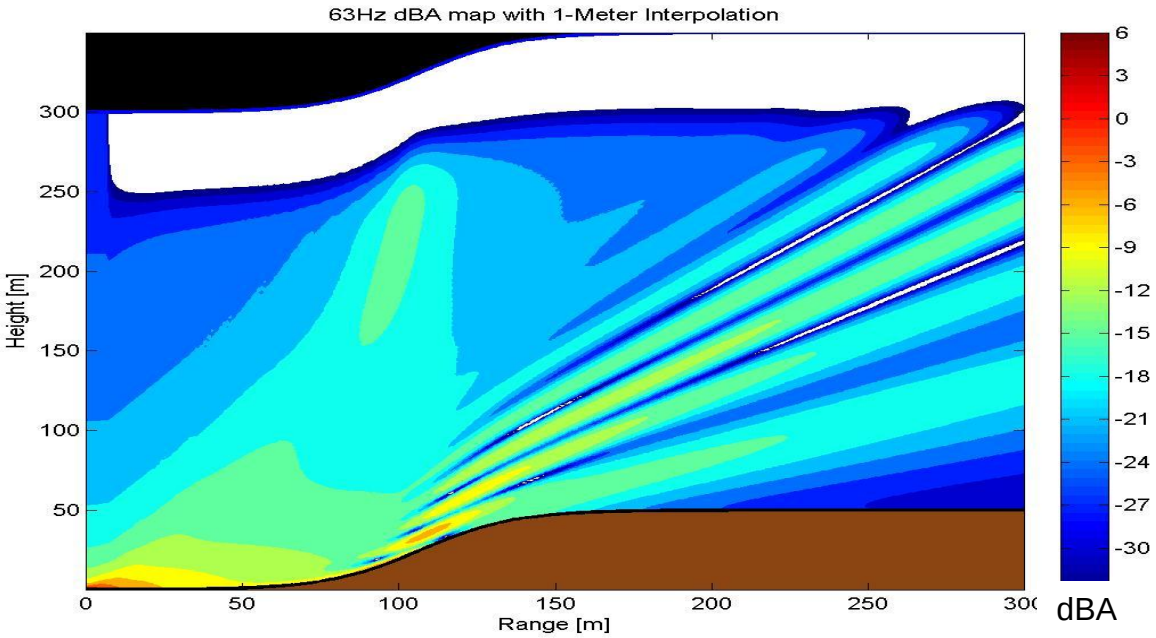

Figure 8. GTPE Case: Escarpment.

Figure 8 shows the GTPE output for a right propagating field from a 63 Hz line source of unit strength at coordinate (0,1) [m] with zero wind and uniform temperature (25^{o}C) interpolated onto a 1 m grid.

II.C.3. Escarpment with Barrier

To explore the effects of placing a wall in the domain, we set the forward pressure field to zero at the wall position to represent a perfectly absorbing wall, thus allowing a determination of the absolute best effect such a wall would have in attenuating the sound field on the far side of the barrier.

II.C.3.1. Model and Domain Setup

The model configuration is the same as described in §II.C.2.1, with the addition of a wall at the top of the escarpment. Keep in mind that the large scale used in the terrain configuration is intended to demonstrate the effects of the terrain. The wall was placed at x_w = 170 m with a height of H_W = 25 m. The height was chosen to knock out the first diffracted constructive lobe pattern. The pressure field at the wall position was set to zero to obtain the best theoretical wall possible.

II.C.3.2. Model Results

The effects of placing a wall are shown in Figure 9. The configuration was the same as for Figure 8, with the addition of a 25 m barrier 170 m from the source position and with zero

transmission. The middle section of Figure 9 shows the terrain profile in meters, and the bottom section shows the sound pressure level at 1 meter AGL versus range.

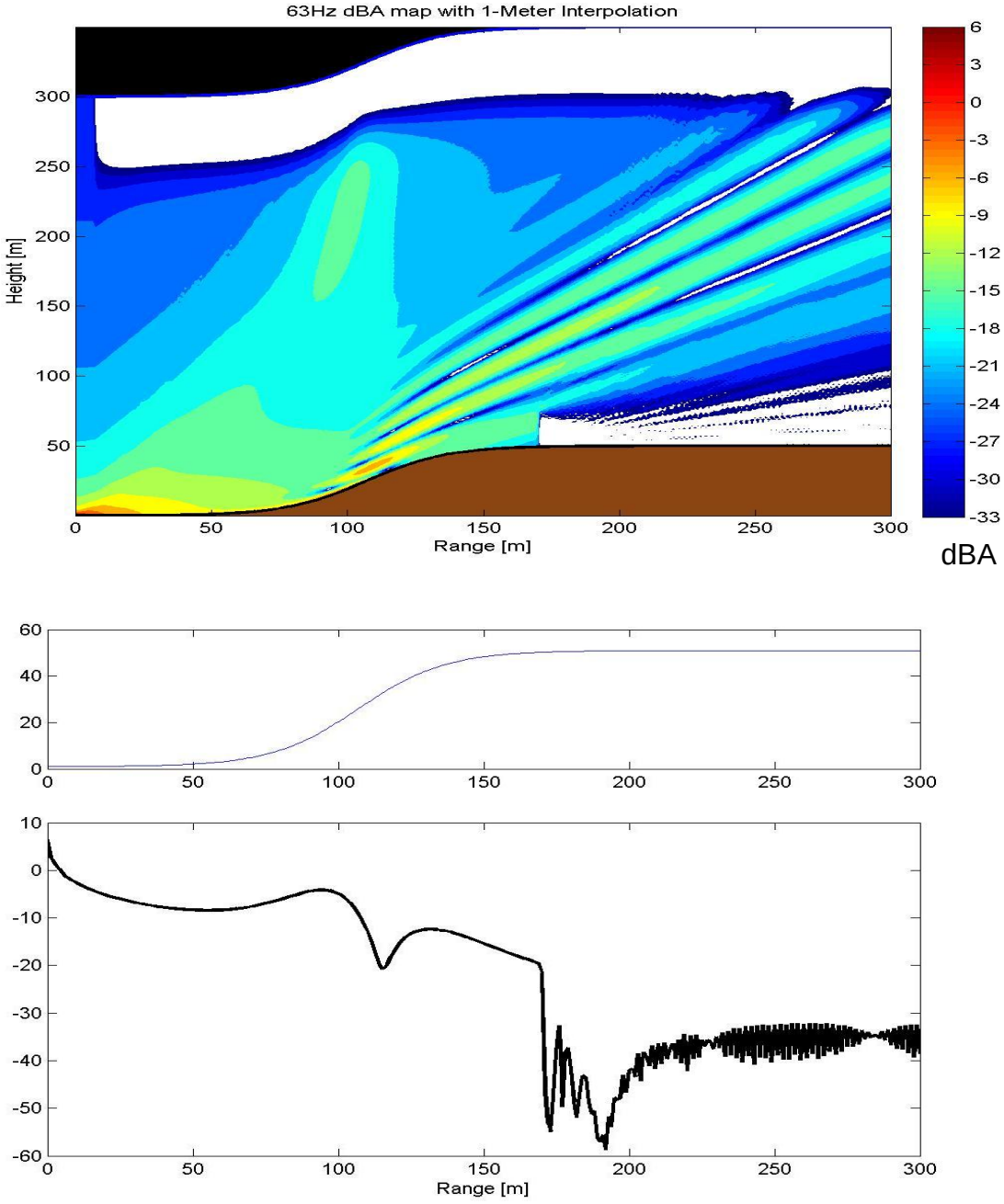

Figure 9. GTPE Case: Escarpment with Barrier. GTPE Output (Top); Terrain Profile (Middle); and Sound Pressure Level at 1 Meter AGL vs. Range (Bottom).

II.C.4. Symmetric Canyon with Barrier and Reflected Field

For the case of a symmetric canyon with barrier and reflected field, we used the incident pressure field from §II.C.3 in Equation 5 to compute a reflected field for the left traveling component of the total field. For this purpose, the impedance was set at $\sigma_W = 10^5$ Pa s m^{-2} so that the barrier would partially reflect the sound.

II.C.4.1. Model and Domain Setup

The domain is identical to that of §II.C.3, except it is symmetric about the origin, extending from -170 m to 170 m from the source. There was no change in the ground impedance to represent the asphalt section, as we want to focus on the reflected field in this neutral case. The starting pressure field for the GTPE model was calculated using the reflected field in Equation 5 up to the top of the wall; from the top of the wall to the top of the domain, it was set to zero.

II.C.4.2. Model Results

For the left running GTPE calculation, we reverse the x coordinate and show the reflected field as starting at x = -170 m and propagating to the right, shown as attenuation relative to the initial starting field (from Figure 9) in Figure 10. Since the outline of the contours is quite jagged, the contour filling patching algorithm could not properly render the image; thus, only the contour levels without solid fill are shown. The reflected field initially decreases in intensity as the waves spread, but then begins to increase in intensity on the far side of the canyon as reflected waves superimpose constructively to refocus the acoustic energy. The net effect results in less than 10 dB attenuation to the symmetrically opposite side of the canyon (seen in the bottom of Figure 10), but nearly 30 dB of attenuation—along with periodic destructive interference drops, or quiet zones—was achieved at the midpoint of the canyon. Subsequent reflections, resulting in reverberation of the sound field between the two walls in a symmetric canyon, could be calculated to determine whether this trend continues with each echo.

Note that the ground impedance remains that of hard sandy soil and does not account for the asphalt section from the starting field of Figure 9. The start and end position of the middle panel is bounded by the reflecting barriers and is symmetric about the origin. The attenuation of the bottom panel is with respect to the original starting field of Figure 9 and is for 1 m AGL.

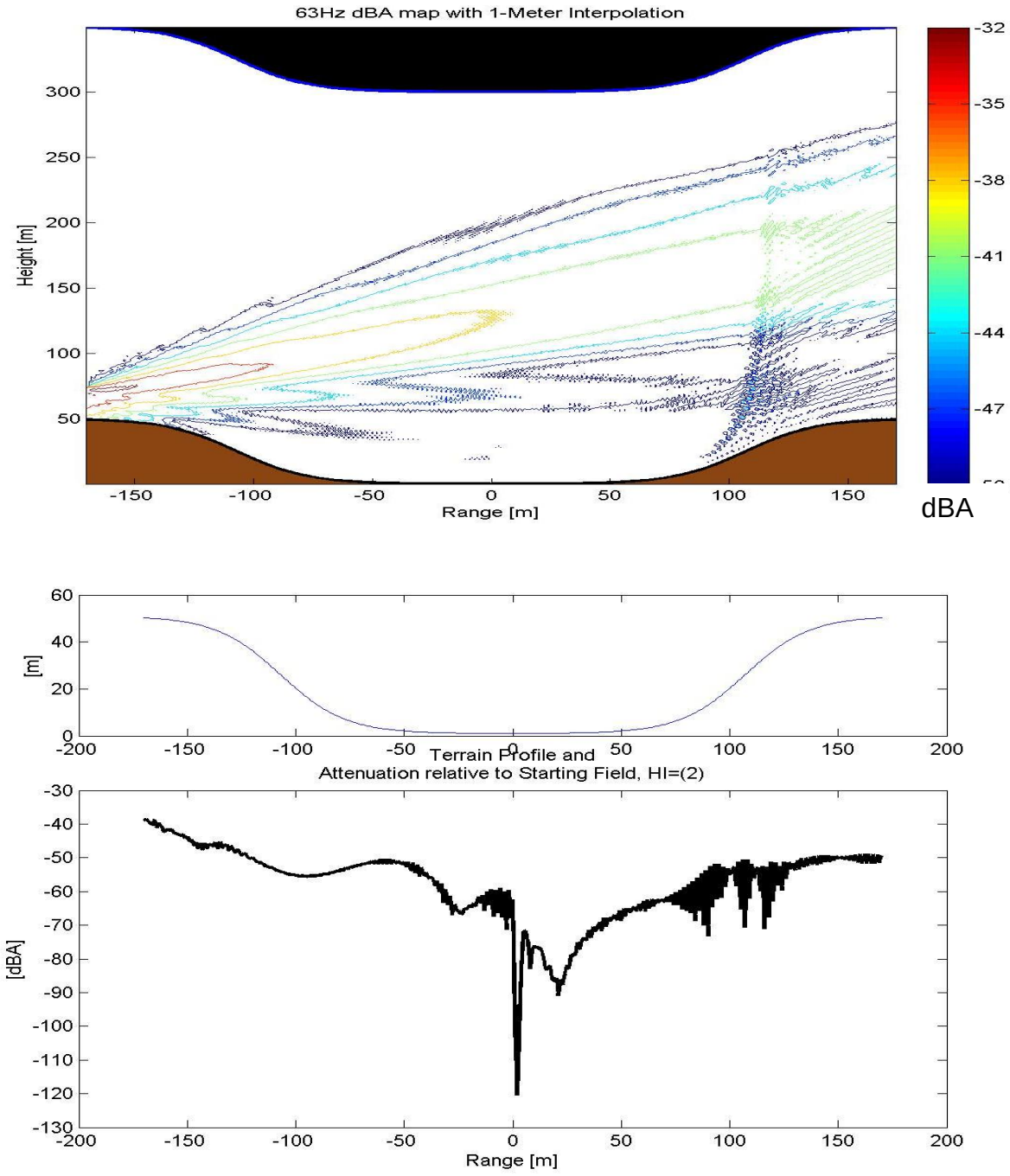

Figure 10. GTPE Case: Escarpment Reflected Field. GTPE Output (Top); Terrain Profile (Middle); and Sound Pressure Level at 1 Meter AGL vs. Range (Bottom).

II.D. DISCUSSION AND CONCLUSIONS

The performance of the GTPE code was demonstrated for a general Gaussian terrain bump and compared against performance for similar terrain that would be expected from Sack and West (1995). A second numerical terrain profile test case was created for a symmetric recessed canyon, both with and without vertical walls placed at the top of an escarpment. Due to the smoothness constraints on the terrain function *H(x)*, and to eliminate artificial numerical diffraction from discontinuities in *H'(x)*, the shape of the canyon was generated with a hyperbolic tangent function (see Figures 9 and 10, middle panel). A routine to determine the reflected pressure wave field from vertically oriented terrain features (e.g., noise barrier walls) was derived from the normal impedance boundary condition and incorporated into the model. Several cases were then run both without and with barriers atop the escarpment for the 63Hz band. In the case with a barrier, the reflected field was then calculated back to a symmetrically opposing barrier. Multiple reflections can be calculated, only after the single reflection is validated. Issues were encountered using the contourf routine in Matlab, believed to be due to a patch algorithm that has difficulties with the irregular contour morphology. Thus, simple contour plots without solid level set filling are presented for the reflected field. Additionally, range plots at 1 meter AGL were generated for all cases. It is difficult to justify summing the incident and reflected fields because the path lengths vary, and it would be difficult to account for the phase of each wave when computing the sum. Instead, the reflected field should be used as a guideline for understanding the intensity of the reflected field and should be presented separately from the incident field. A worst case could then be constructed by summing the magnitudes of the two fields, accounting for phase by distance along the ground from the source, including reflected distances.

II.E. FUTURE WORK

In the review of Li et al. (1993), a method was proposed for determining the analytical prediction of sound field over a terrain with a Gaussian-shaped hill in the presence of a uniform or linearly varying sound speed profile. The method substitutes a Green's function solution for the field from a line source into the Helmholtz-Kirchoff integral equation, yielding an exact closed form solution. This method could be extended for the hyperbolic tangent terrain profile without barrier for comparison with the neutral cases presented herein. Literature was reviewed to find methods for benchmark comparisons and calculations of diffraction from simple terrain features. Some potentially useful publications include Gauvreau et al. (2002), Robertson (1999), Rasmussen (1985) and Bowman and Thomas (1987).

Additionally, a formulation was derived for calculating the backscattered field from terrain with arbitrary angles and for barriers with facades tilted slightly from vertical. The formulation is similar to that derived for vertical barrier reflection, resulting from combining the first order parabolic equation operator with the normal impedance ground boundary condition of Sack and West (1995). A numerical implementation has been outlined and will soon be applied. Computational fluid dynamics software such as FLUENT could be used to generate simulated input meteorological fields for cases of flow over fine terrain.

III. NOISE FORECASTING MODEL

The organization of this chapter is as follows:

- An introduction to and motivation for this study are briefly discussed in §III.A.
- The sound model numerical experiment is presented in §III.B, with the WRF configuration given in §III.B.1, a description of the sound model in §III.B.2, the selection process for WRF profiles in §III.B.3, the profiles themselves in §III.B.4, and results of the sound model in §III.B.5.
- These sections are followed by discussion and conclusions in §III.C and suggestions for future work in §III.D.

III.A. INTRODUCTION

The Weather Research and Forecasting (WRF) model (Skamarock and Klemp 2008; Skamarock et al. 2008) is a state-of-the-art compressible non-hydrostatic Navier-Stokes or Euler equation solver specifically applied to terrestrial atmosphere modeling using mass-based coordinates. Development of this open-source community code is centered at the Mesoscale and Microscale Meteorology (MMM) division of the National Center for Atmospheric Research (NCAR). The latest version of the Advanced Research Weather Research and Forecasting model (Skamarock and Klemp 2008) is ARW-WRF v3.2, released on 31 March 2010. ARW-WRF v3.2 can refine the vertical grid resolution within a child domain, making possible the study of detailed phenomena and enabling further application of the model output data in a limited area without the computational expense of running all nests at the higher resolution (Mahalov and Moustaoui 2009). The model was previously capable only of nesting horizontally to refine resolution within a specific geographical region, but with all child domains, or nests, using the same vertical grid.

It is desirable to forecast these profiles both for future studies and for reanalysis of previous studies that may have not accounted for the full meteorological profile. Additionally, forecasting makes it possible to base long-term noise pollution assessments on refractive atmospheric conditions of the near-ground, high-resolution profiles. We demonstrate the degree of representativeness that can be attained from utilizing vertical nesting to 81 levels from 27, at 1 km horizontal resolution, in comparison with results of meteorological profile Case A from Ovenden et al. (2009) during representative stable morning inversion conditions. Stable inversions have been difficult to resolve with previous meteorological forecasting models, especially to the degree necessary for satisfactory application to studies of noise pollution with reasonably available computational resources.

III.B. SOUND MODEL NUMERICAL EXPERIMENT

To explore the possibility of forecasting the sound field by coupling the GTPE model capability with meteorological fields generated by an external model, we a numerical test case was developed using the WRF model. As a first step to validate the forecast capability, the PE model

was used to compare with results from Ovenden et al. (2009). The WRF model version 3.1 was downloaded and compiled to run jobs on the ASU-Fulton Saguaro computer cluster. Several practice cases were run to gain familiarity with using the WRF model with the Advanced Research WRF (ARW-WRF) core. Version 3.2 of the WRF model (released on April 2, 2010) was then installed, which allows for higher resolution vertical nesting and, hence, a resolution comparable to observational input profiles previously used for the PE sound model.

For a comparison case, the 2006 field experiment dates of November 7 and 8 at the Loop 202 site were chosen. Figure 11 shows the WRF model domain.

III.B.1. WRF Model Domain

Figure 11. The WRF Model Domain (Generated Using WRF Domain Wizard).

The domain shown in Figure 11 consists of four nests centered on Phoenix, Arizona, with horizontal resolutions of 27, 9, 3 and 1 km, and horizontal size of 100, 134, 182 and 254 grid cells for domains 1, 2, 3, and 4, respectively. All domains are centered on Phoenix, with the outer domain centered at coordinates (33.45 N, -112.074 W). However, due to grid spacing issues while nesting, the finest grid is centered on coordinates (33.8008 N, -111.6519 W). The three parent domains have 27 vertical levels and the fourth has 81, as illustrated in Figures 12 and 13.

All nests were spaced between 1000 and 50 mb, where 1 bar was taken as surface pressure. The dimensionless vertical coordinate used in hydrostatic simulations is called a sigma level,

with the coordinate transformation from pressure given by $\sigma = \frac{P_h - P_{ht}}{P_{hs} - P_{ht}}$, also called a mass vertical coordinate. The mass vertical coordinate varies between 0 and 1, depending on the value of the hydrostatic pressure P_h in comparison to the surface and model top hydrostatic pressure values, P_{hs} and P_{ht}, respectively (Skamarock et al. 2008). The pressure-based vertical coordinate, $Z^{(P)}$, arises from the solution of the hydrostatic relation as $Z^{(P)} = H \ln(P_{hs}/P_h)$, where H = 6.5 km is a scale height. The more accurate vertical coordinate Z, which is actually used for profiles, is related to the geopotential φ by the gravitational constant g, namely $\varphi = gZ$, where the WRF model gives output in terms of the perturbation plus base state geopotential, $\phi = \phi' + \bar{\phi}$. The results of refining the nest on the sigma levels is demonstrated in Figures 12 and 13, with the lowest values used for profile heights summarized in Table 1.

Table 1. Lowest Grid Point Values Showing the Correspondence Between Vertical Level (n), Sigma Value (σ), Pressure (P), Height Above Ground Based on Pressure (Z(P)), and Height Above Ground Based on Geopotential (Z) for the Vertically Nested with Increased-Resolution (81 levels) and Coarse-Resolution (27 levels) Nests Denoted by How Many Vertical Levels Are Used in the Domain.[a]

81 vertical levels					27 vertical levels				
n	σ	*P* [mb]	$Z^{(P)}$ [m]	*Z* [m]	*n*	σ	*P* [mb]	$Z^{(P)}$ [m]	*Z* [m]
1	**1.000**	**1000**	**0.0**	**0.0**	**1**	**1.000**	**1000**	**0.0**	**0.0**
2	**0.997**	**997**	**14.4**	**19.2**	**2**	**0.993**	**993**	**43.4**	**57.9**
3	**0.995**	**995**	**28.9**	**38.4**	**3**	**0.983**	**984**	**105.8**	**141.4**
4	**0.993**	**993**	**43.4**	**57.7**	**4**	**0.970**	**972**	**187.9**	**250.9**
5	**0.990**	**990**	**64.1**	**85.4**	**5**	**0.954**	**956**	**290.4**	**387.4**
6	**0.986**	**987**	**84.9**	**113.1**	**6**	**0.934**	**937**	**420.9**	**560.7**
7	**0.983**	**984**	**105.8**	**141.0**					
8	**0.979**	**980**	**133.1**	**177.2**					
9	**0.974**	**976**	**160.5**	**213.7**					
10	**0.970**	**972**	**187.9**	**250.2**					
11	**0.965**	**966**	**221.9**	**295.4**					
12	**0.959**	**961**	**256.1**	**340.9**					
13	**0.954**	**956**	**290.4**	**386.5**					
14	**0.947**	**950**	**333.6**	**443.9**					
15	**0.941**	**944**	**377.1**	**501.6**					

[a] Higher-resolution nests can be generated, but with increased computation time and in need of increased horizontal refinement, which would require higher-resolution geographic input data for the WRF preprocessing model (WPS).

For this study, the physics and dynamics options were set to the values provided in Appendix B.[1] Since there were no complex cloud conditions, we selected the WSM 3-class microphysics option along with the Kain-Fritsch cumulus option every 5 minutes. We used the RRTM long-

[1] Some of these values are explained in this document, but the reader is strongly encouraged to review Skamarock et al. (2008) for further details.

wave and Dudhia short-wave radiation schemes called every 30 minutes. The Monin-Obukhov surface layer scheme was used with thermal diffusion and the YSU planetary boundary layer (PBL) and without the urban physics option.

Initial conditions were derived from interpolating the standard 1° Global Forecast System model data provided every 6 hours by the National Center for Environmental Prediction.[2] Land classification was derived from the 30 arc-second resolution (~1 km) moderate resolution imaging spectrometer (MODIS)[3] geographical data (available for download on the WRF users' website).[4]

For the fourth domain, the model was initially configured to run for 42 hours beginning at 6 p.m. on November 5, 2006, to allow sufficient model spin-up time. The finish time for the fourth domain was set at noon on November 7, and the larger domains were computed until noon on November 8. The run time for just the high-resolution nest was approximately 3,220 computer hours; the run was performed on 128 Intel Xeon quad-core processors in just over 25 Earth hours for the 42 hours of simulated time.

It was later realized that the model time is in universal standard time (UTC, aka Zulu or Z), not local standard, which for Arizona corresponds to -7 UTC. The model stop time of noon thus results in a local stop time of 0500, so a direct comparison with previous work was not possible; instead, the model run was used as a guide for morning conditions and Ovenden's Case A was selected. For this reason, Appendix C shows the Ovenden et al. (2009) cases for comparison. Future work will include re-running these cases for the correct times in addition to varying the PBL and surface layer schemes. Additionally, we only show comparisons between the 3 km horizontal grids with 27 vertical levels and the 1 km horizontal grids with 81 vertical levels. Future work will include 1 km horizontal with 27 vertical levels.

Figures 12 and 13 illustrate the non-uniform vertical grid spacing used in the WRF model with 27 vertical levels in the three large nests and 81 vertical levels in the fourth nest. These figures show the correspondence between grid sigma level (a dimensionless vertical coordinate) and height above ground based upon pressure ($Z^{(P)}$) in meters (top plot in each figure) and pressure in mb (bottom plot in each figure) for the entire vertical extent of the simulation domain of 1000 to 50 mb. The solid blue downward-pointing triangles represent the coarse grid points used in domains with horizontal grid spacing of 3, 9, and 27 km, and the open upward-pointing triangles represent the levels for the vertically refined fourth nest, which has 1 km horizontal spacing.

[2] The data for this study are from the Research Data Archive (RDA), which is maintained by the Computational and Information Systems Laboratory (CISL) at the National Center for Atmospheric Research (NCAR). NCAR is sponsored by the National Science Foundation (NSF). The original data are available from the RDA (http://rda.ucar.edu) in dataset number ds083.2.

[3] Information on the MODIS data can be found at http://modis.gsfc.nasa.gov/about/

[4] The WRF users website: http://www.mmm.ucar.edu/wrf/users/download/get_sources.html

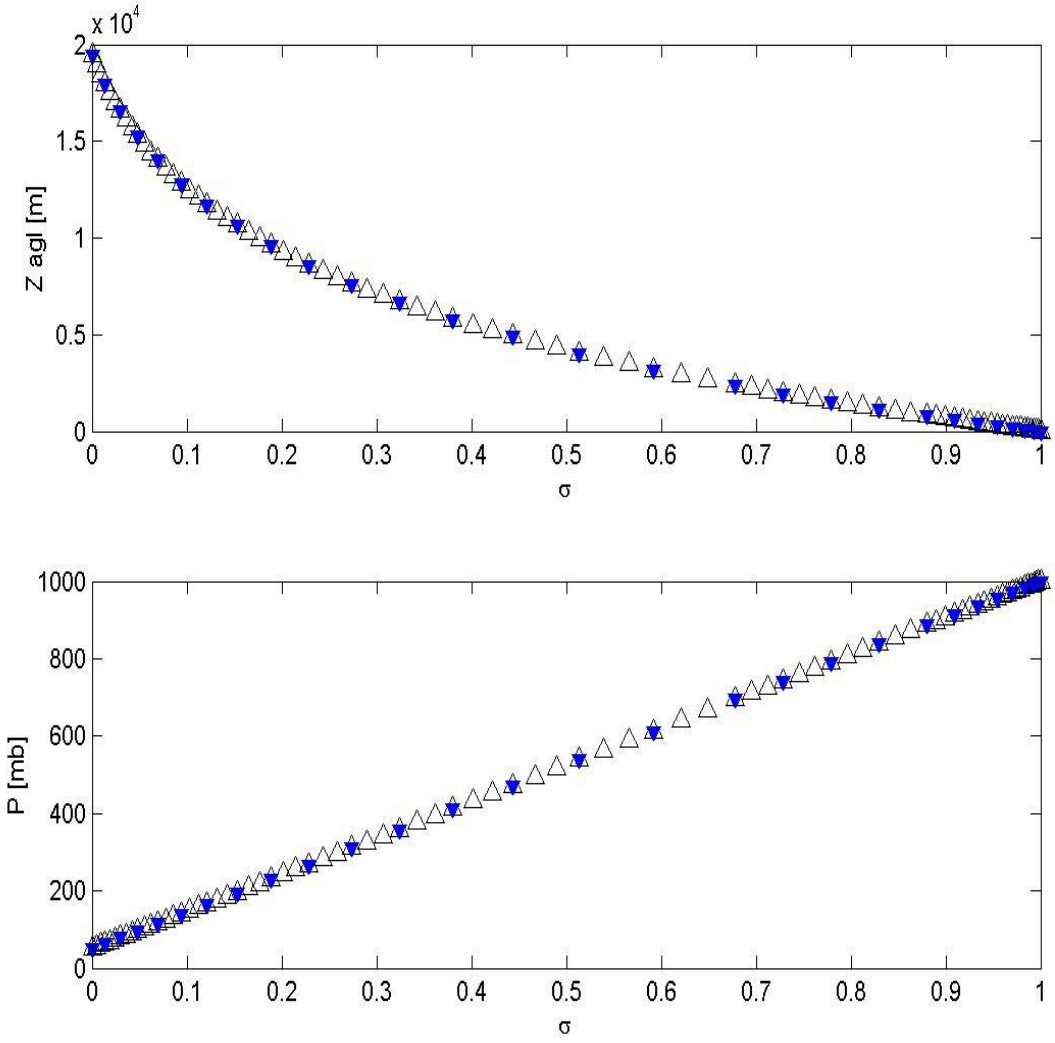

Figure 12. WRF Vertical Grid Spacing.

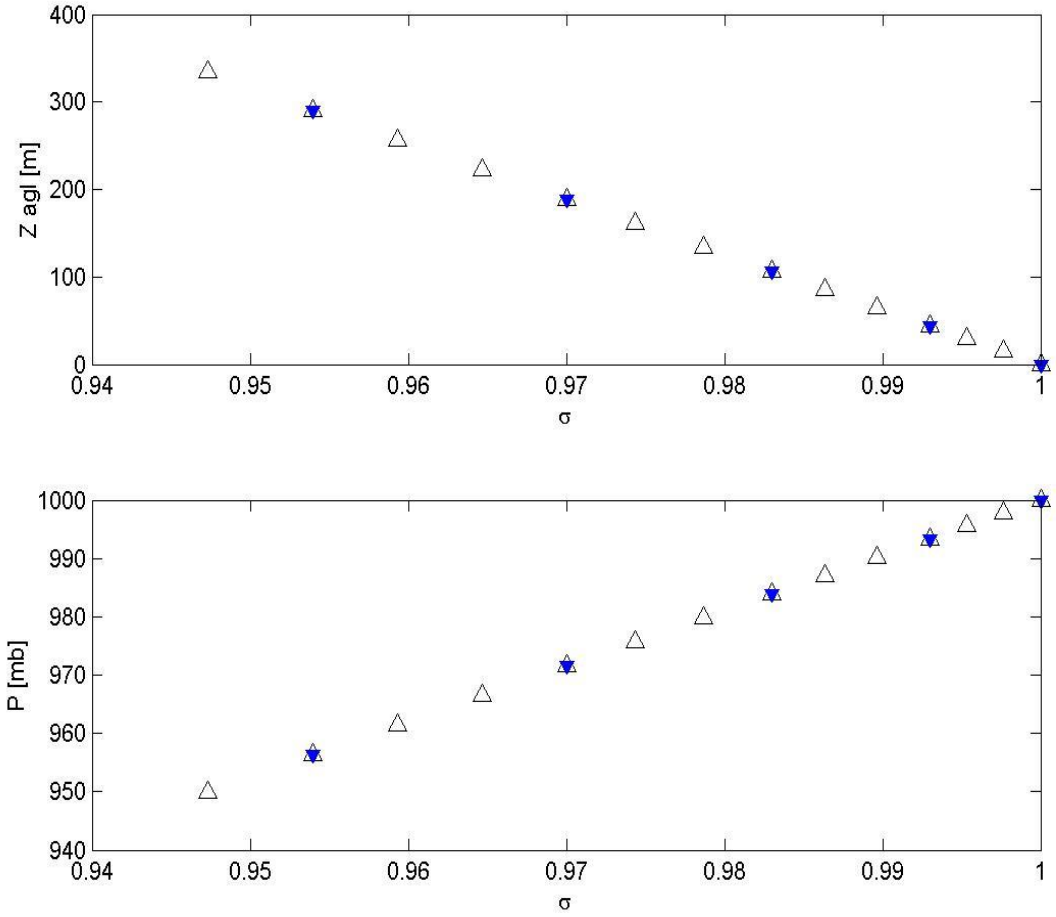

Figure 13. WRF Vertical Grid Spacing Zoom.

Figure 13 is the same as for Figure 12, only zoomed in near ground level for the lowest ~300 m. Further detail is shown in Table 1.

III.B.2. PE Sound Model

To demonstrate that we can reconstruct input meteorological profiles with WRF and evaluate the resultant sound field for comparison with previous work, we begin with the flat terrain model used in the prior study by Ovenden et al. (2009). That model is briefly summarized as follows:

The highway is treated as a series of single-frequency coherent effective line-sources above a fixed lane, a reasonable approximation when considering 20-minute time-averaged sound levels. The ground is treated as an impedance plane using flow resistivity values representative of asphalt and hard sandy soil in the one-parameter model of Daleny and Bazley (1970). A spectral model called the wide-angle Parabolic Equation (PE) approximation (Salomons 2001) is

used to model one-way sound propagation from a profile of complex pressure deviations from mean pressure. The PE model is derived by splitting the 2-D Cartesian Helmholtz wave equation into two one-way propagation operators and considering only waves moving in one direction within a 2-D plane transverse to a line source. An absorbing layer at the model's top boundary prevents artificial numerically reflected waves.

Stability of the PE model requires 10 points per wavelength, so high frequencies become costly to compute. Restricting the acoustic spectrum to 17 standard third-octave frequency bands incurs less than 1% error due to A-weighting when compared to the sum over any larger bandwidth and speeds computation time by eliminating higher frequencies. Each third-octave band's central frequency is assumed to represent the entire band, so the logarithmic-sum of the PE calculations for each band gives the resultant total field.

The model input is the starting pressure field and the effective-sound-speed profile up to 300 m AGL, defined as

$$C_{eff}(z) = C_{ad} + U_{||}(z) \qquad \text{(Eq. 12a)}$$

$$C_{ad} = \sqrt{\gamma RT(z)}\ , \qquad \text{(Eq. 12b)}$$

where γ is the ratio of specific heats, *R* is the gas constant, *T(z)* is the temperature profile, and $U_{||}(z)$ is the profile of fluid flow speed parallel to the direction of propagation. The first term, given by Equation 12b, is commonly referred to as the adiabatic sound speed. Upon substituting constant values for dry air, C_{ad} is given by $C_{ad}(z)$=331.3 ($T(z)$/273.15)^.5 m s^{-1} where the temperature, *T,* is in Kelvin. The second term in Equation 12a accounts for advection by approximating the medium as being stationary and adding the medium motion in the direction of sound propagation. The source heights and strengths were kept the same as for Case A in Ovenden (2009). See Appendix C. A Green's function solution for an infinite line above an impedance plane is used to obtain the starting pressure field for the PE model at the edge of the roadway, where the ground impedance value changes from one representing asphalt to one representing hard sandy soil. The model configuration is identical to that used in Ovenden (2009). Atmospheric absorption is applied to each frequency band after the PE model gives output.

III.B.3. Site Location and Profile Selection

The site used for previous studies in Ovenden (2009) is adjacent to highway Loop 202 in the East Phoenix Metropolitan area at approximately 33.48240 N latitude and 111.76338 W longitude (denoted in Figure 14a and 14b by a blue marker). The schematic in Figure 14a for the 1 km resolution WRF grid center locations shows the two closest points in green, nine of the ten nearest neighbors in yellow, and the nearest remaining grid location for the 3 km nest in red. Note that both grids are coincident at this point. These locations are overlaid on a Google Earth image in Figure 14b to give an indication of the land use for this area.

Based upon these grid locations, and with the highway running primarily East-West, profiles of potential temperature and V velocity are extracted to generate the $C_{eff}(z)$ profiles used for input to the PE model. We denote by C^{-}_{eff} when looking against the V component of the wind, or in the negative-y direction (e.g., in general, $C^{\pm}_{eff} = C_{ad} \pm V$). Thus we can look for effects in a downward refracting medium in order to better understand high noise level events and to explore mitigation strategies.

The computational grid used in the WRF model, called an Arkawa-C staggered grid (Skamarock et al. 2008), places vector quantities, such as velocity, at the cell boundaries. Scalar values such as potential temperature, however, are computed at the cell centers. For the purposes of this study, we take the profiles corresponding to the same grid coordinates in computing the effective sound speed profile, but note that the velocities are actually displaced by half the grid cell dimension (to the North for the V-component). We also note that the output of the WRF at each hour is in local ("instantaneous") values, while 20-minute time-averaged profiles were used in Ovenden's previous work (2009). For this reason, and because of the turbulent nature of the flow, we choose not only the profiles at the two grid locations closest to the site of interest, but also a set of nearest-neighbor sites, to build an ensemble of profiles representative of that region at the given time. One might then be led to invoke Taylor's hypothesis that spatial averages at an instant of time are equivalent to time averages at a fixed location for direct comparison with the previous work (Stull 1988). However, this flow is neither homogeneous nor isotropic. Therefore, we will view the variations in the profiles as sampling from the true distribution, but will place more emphasis on the two points closest to the site location by making them bold in Figures 15–17, and showing the near-neighbor profiles as subdued dashed curves. This illustrates the variability in the profiles for that region at the time of model output and shows the degree of representativeness of the resultant attenuation versus range plots, with the dashed curves giving an estimate of the variance and the solid curves giving a realization closest to the site location.

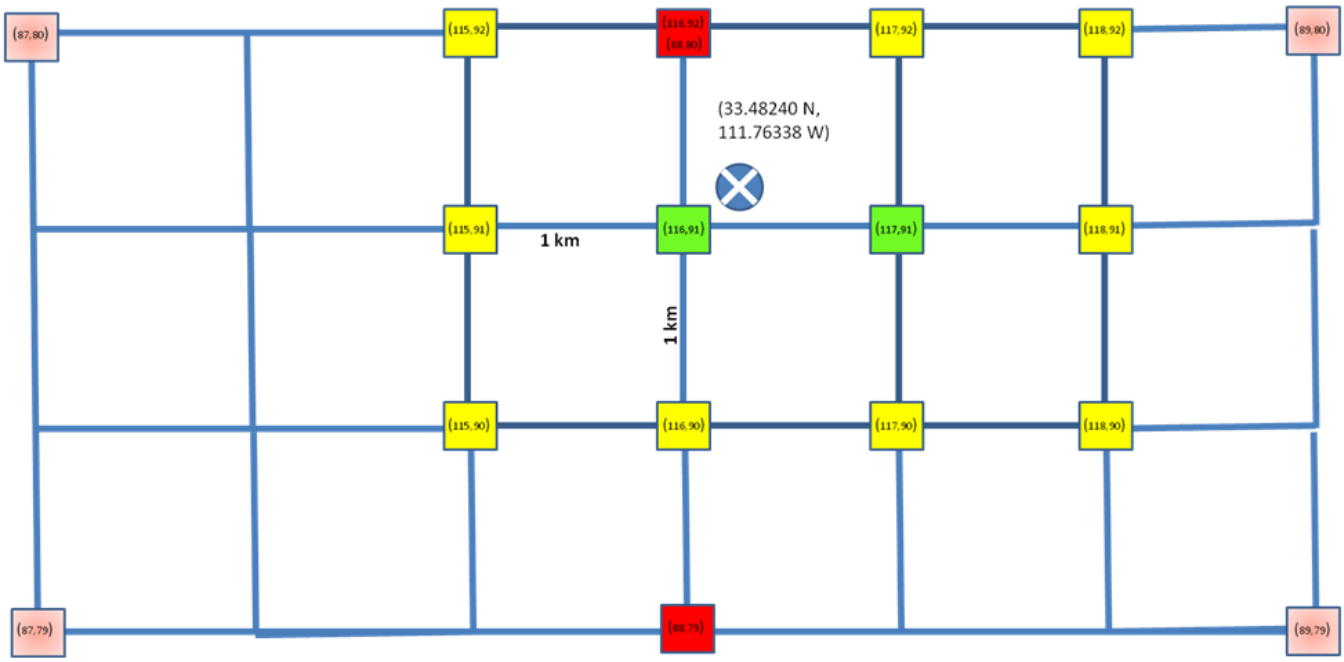

(a) Schematic

(b) © 2006 Google Earth background

Figure 14. WRF Grid Near Site Location.

In the figure above, the subset of WRF computational domain for the Arkawa-C staggered grid cell center locations in the neighborhood of the site location defining the numerical study area is shown (blue, with approximate latitude and longitude) as a schematic (a) and with Google Earth background (b). Squares (a) or pins (b) indicate x-y coordinates of the nearest WRF grid points for the 1 km horizontal grid (green) and 3 km horizontal grid (red), along with nearest-

neighbor grid points on the 1 km grid (yellow) and the 3 km grid (pink). North is up for both figures.

III.B.4. Input Meteorological Profiles Derived from WRF

Case B in Ovenden (2009) is between 7:40 a.m. and 8 a.m. local time on November 7, 2006. The WRF run was begun at UTC 0500 on November 5, 2006, to allow sufficient spin-up time. Profiles were then extracted at 1200 UTC on November 7, 2006, as representative of the morning inversion, and used to derive C_{eff}. The temperature was obtained by

$$T = (\theta' + \theta) \times \left(\frac{P' + \overline{P}}{P_0}\right)^{R/c_p} , \qquad \text{(Eq. 13)}$$

where θ=300 K is the base potential temperature, θ' is the perturbation potential temperature, P_0=10^5 Pa is the reference pressure, $P' + \overline{P}$ is the perturbation plus base pressure, and R/c_P=8.314472/29.07 is the ratio of the gas constant to the specific heat at constant pressure for dry air.

Using Equation 13 in Equation 12 along with the definition of adiabatic sound speed, the profiles of C_{eff} were derived. Figures 15 through 17 show the profiles of V (positive to the North), C_{ad}, and C_{eff}, respectively. In each of the profile plots, the right panel shows the full 20 km vertical extent, and the left panel shows only the 400 m nearest the ground. The red line corresponds to the 27 vertical level profiles on the 3 x 3 km grid (red points in Figure 14), and the black line corresponds to the 81 vertical level profiles on the 1x1 km grid (green points). The black dashed lines represent the nearest neighbors in the 81 vertical level resolution, and the red dashed lines show them in the 27 vertical level resolution. Vertical levels are indicated by green squares (lowest 13 of 81) and red circles (lowest 5 of 27) in the left panel only for the two profiles closest to the site. Before these profiles can be used in the sound model, they are interpolated with a cubic spline routine (csape in Matlab) to the resolution needed for each frequency to maintain 10 points per wavelength. Appendix B provides profiles of the derived temperature T, along with other supplementary profiles derived from the WRF model (θ, U, W).

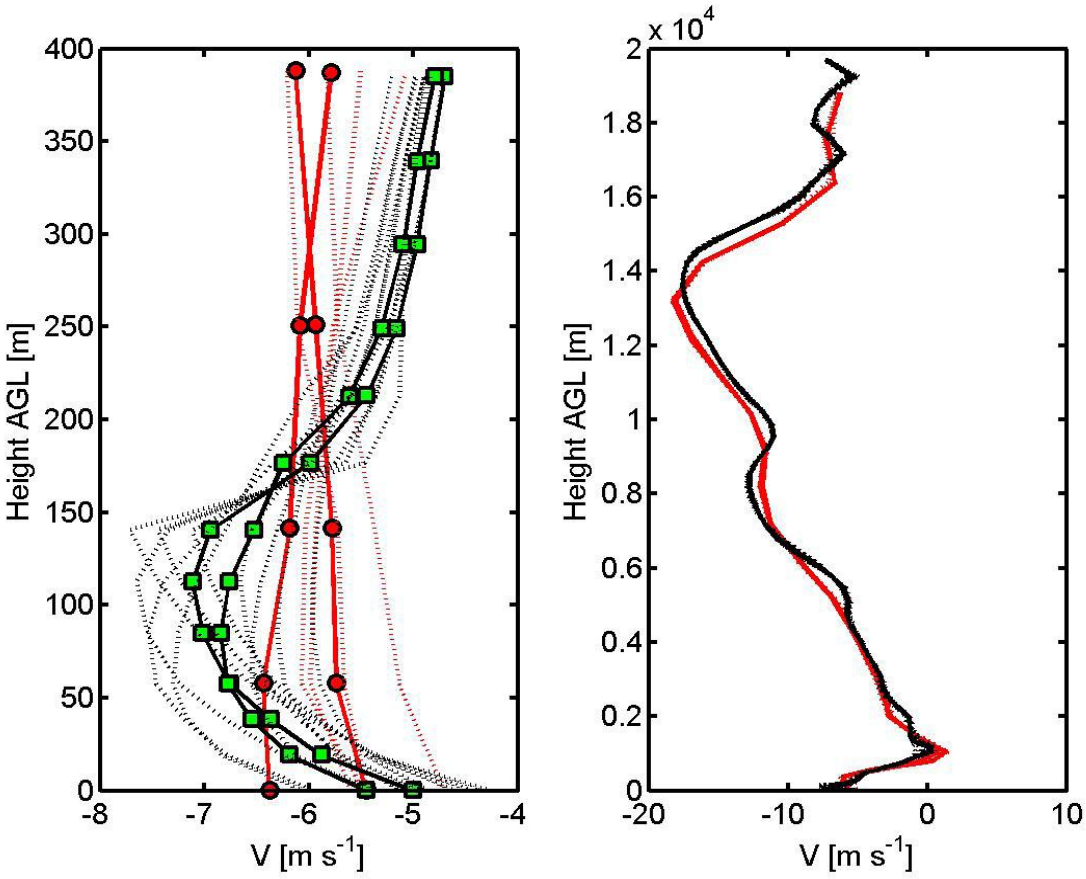

Figure 15. WRF Profiles of V Component of Velocity.

Figure 16 is the same as Figure 15, but the profiles here are for the adiabatic sound speed derived from potential temperature using Equations 12 and 13.

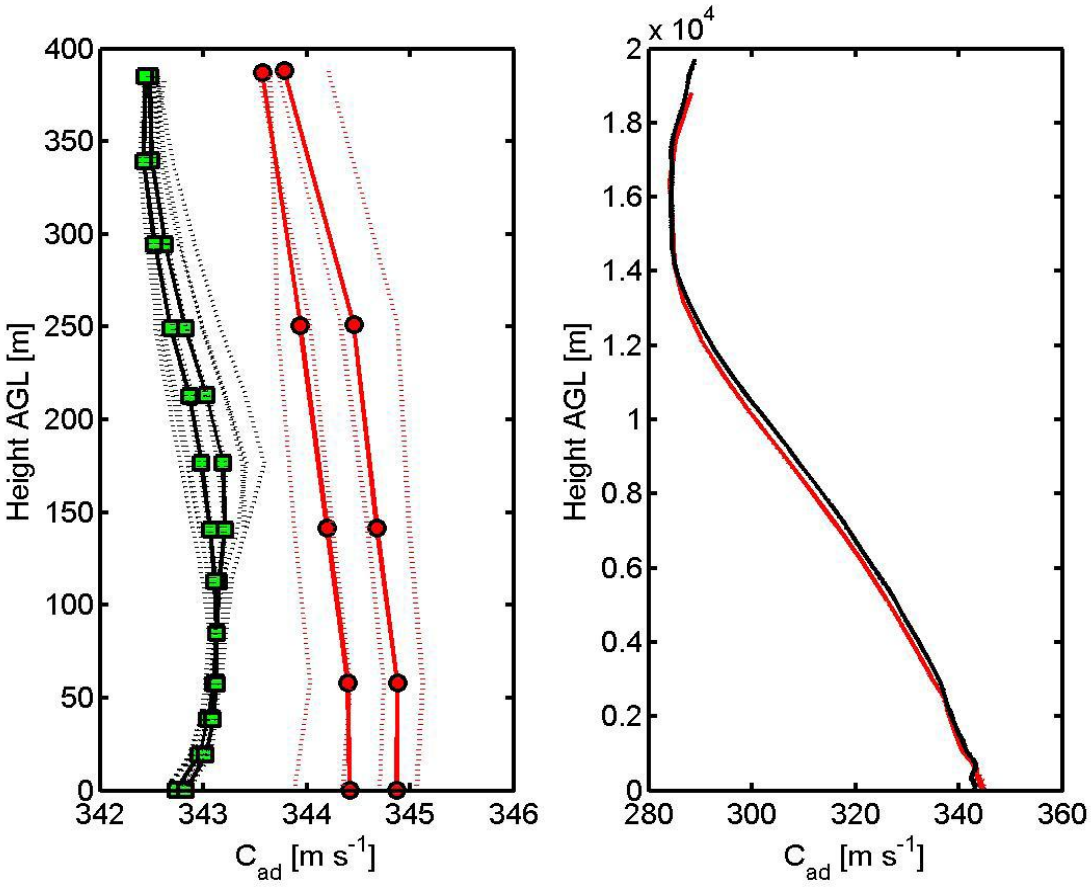

Figure 16. WRF Profiles for Adiabatic Sound Speed.

Profiles here are the same as for Figure 15 but for C_{eff} looking downwind towards the south side of the highway.

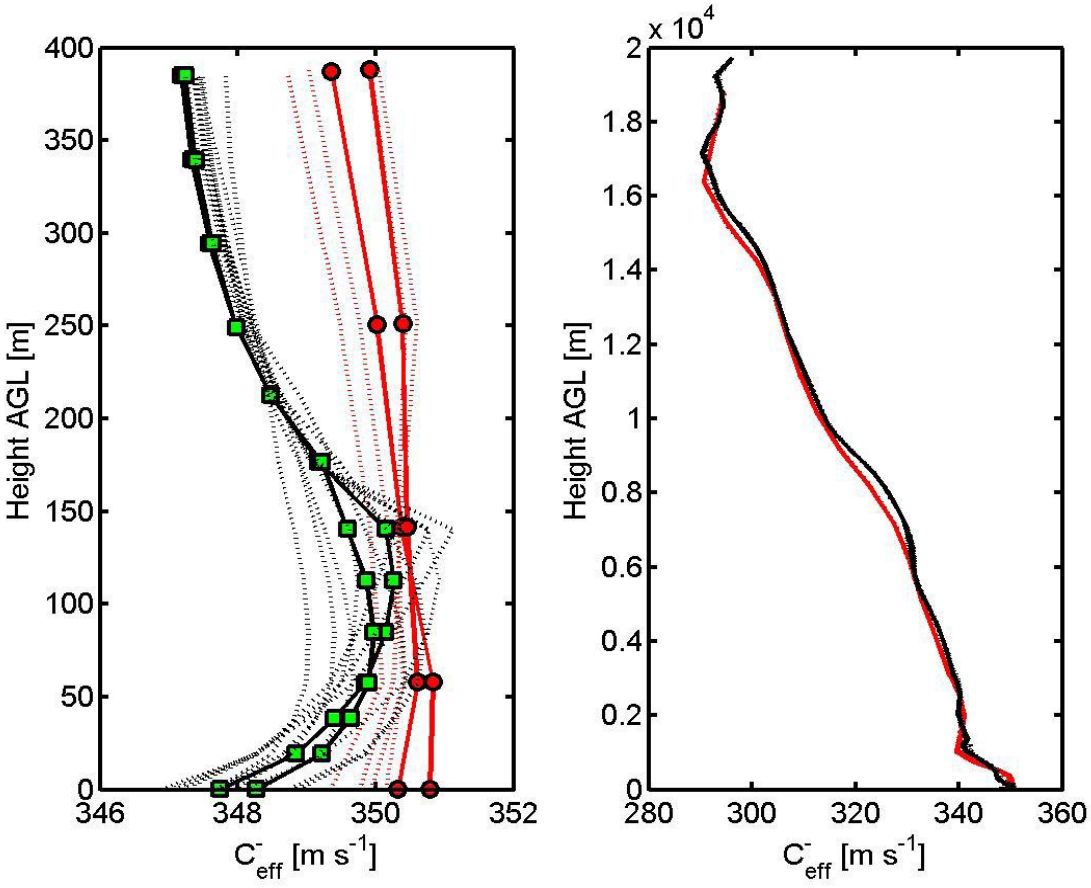

Figure 17. WRF Profiles of Effective Sound Speed

III.B.5. PE Model Results

The PE model was used to calculate the total sound field based upon the C_{eff} profiles extracted. A spectrum versus range at 1 m AGL was then obtained for the central frequency of the 17 third-octave bands. These figures are useful for determining the near-ground influence of the refractive medium on the propagation of the source with a given spectral intensity distribution. Figure 18 shows the neutral case, a control where the velocity is set to zero and the temperature profile is held fixed at the ground value. The study conducted by Ovenden et al. (2009) emphasized the difference between the neutral case and a case using C_{eff} profiles. Here, we see the benefit of increased model resolution for forecasting C_{eff} profiles when comparing the spectral-range plots for the 27 and 81 vertical levels of C_{eff} closest to the site location (Figures 19 and 20) to the results from Ovenden's Case A (Figure 21, showing morning conditions).

The sound pressure level (SPL) for a given frequency band n, in a time-averaged sense, is denoted by $L_{eq,n}$ and was computed by

$$L_{eq,n}(x,z) = 10\log_{10}\left(\tfrac{1}{2}|P_n(x,z)|^2 + S_n^2 - |x|\alpha_n\right), \quad \text{(Eq. 14)}$$

where P_n is the complex pressure amplitude, S_n is the source strength, and α_n is the attenuation coefficient. For the spectrum versus range plots, Equation 14 was evaluated at *z=1* m AGL. The total SPL, denoted L_{eq}, can be computed by taking the logarithmic sum over all frequency bands by

$$L_{eq}(x,z) = 10\log_{10}\sum_{\mathrm{n=1}}^{17} 10^{\mathrm{L_{eq,n}}(x,z)/10}. \quad \text{(Eq. 15)}$$

Attenuation is typically calculated as the difference between the SPL at two positions in range, so we compute this difference with respect to the value at 50 m range as follows:

$$A(x) = \tilde{L}_{eq}(x, z = 1\ \mathrm{m}) - \tilde{L}_{eq}(x = 50\ \mathrm{m}, z = 1\ \mathrm{m}), \quad \text{(Eq. 16)}$$

where here the evaluation at *z* = 1 m AGL has been made explicit. However, to remove the bias between the profiles owing to their different ground level C_{eff} values, the respective neutral case PE model calculations—in which only the ground level temperature contributes to C_{eff}—are used to shift each calculated field with the full C_{eff} profile to a common baseline (hence the tilde over the symbol *L*). Thus the $\tilde{L}_{eq}$ values in Equation 16 also include the terms

$$\Delta L_{eq}(x, z = 1\ \mathrm{m}) = L_{eq}^{[n,r]}(x, z = 1\ \mathrm{m}) - L_{eq}^{[n]}(x, z = 1\ \mathrm{m}) \quad \text{(Eq. 17)}$$

to account for this bias compared to what would be computed using Equation 15, as $\tilde{L}_{eq} = L_{eq} + \Delta L_{eq}$, where superscripts within []'s of n refer to the neutral SPL value and r to the

chosen reference profile, which for this case corresponds to the neutral profile from Case A in Ovenden et al. (2009).

Finally, to comparatively display the degree of representativeness between the resultant sound fields for the various $\bar{C}_{eff}$ profiles used, we show an attenuation versus range plot at 1 m AGL, which displays the near-ground response of the atmosphere for a given source relative to the reference position. The bias or offset subtraction ensures that all attenuation-versus-range plots have the same zero point, so direct comparisons of the results shown in Figure 22 can be made.

Figure 18 shows the A-weighted spectrum [dBA] versus range plotted at 1 meter AGL. Here the neutral case, defined as using a constant ground-level temperature and zero wind in Equation 12, was derived from the experiment having 27 vertical levels and a 3 km horizontal grid spacing." The 81 vertical level neutral case (not shown) is similar (because the vertical gradient is also zero) but shifted, because a different temperature gave a different uniform adiabatic sound speed. Contours are in intervals of 3 dBA, consistent with a doubling of distance from a line source, yielding half of the sound pressure level.

Figure 19 is the same as Figure 18 except the WRF simulation with 27 vertical levels and 3 km horizontal spacing were used to derive the $\bar{C}_{eff}$ profile (in Equation 12). Figure 20 is the same as Figure 19, except the WRF simulation uses 81 vertical levels with 1 km horizontal spacing to derive the profiles of $\bar{C}_{eff}$. Figure 21 is also the same as Figure 19, except the C_{eff} profile from Case A of Ovenden (2009) is used.

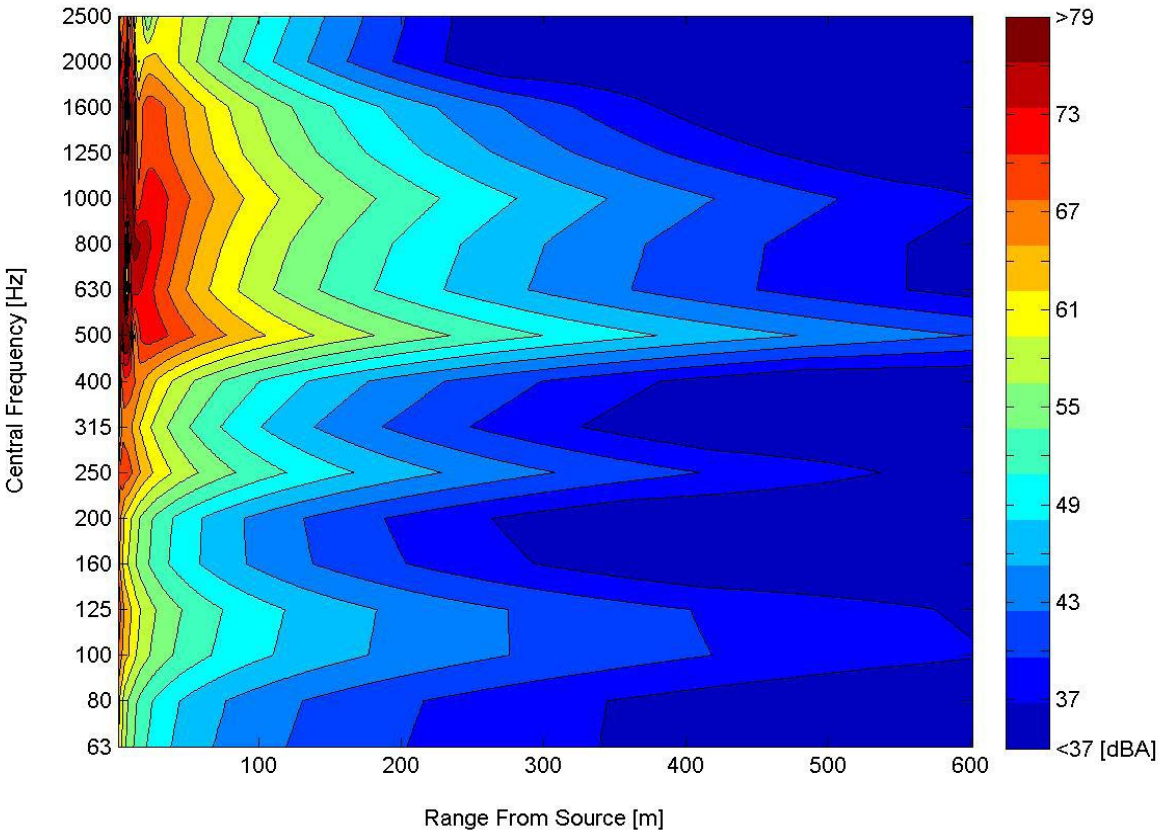

Figure 18. Spectrum vs. Range–Neutral Case.

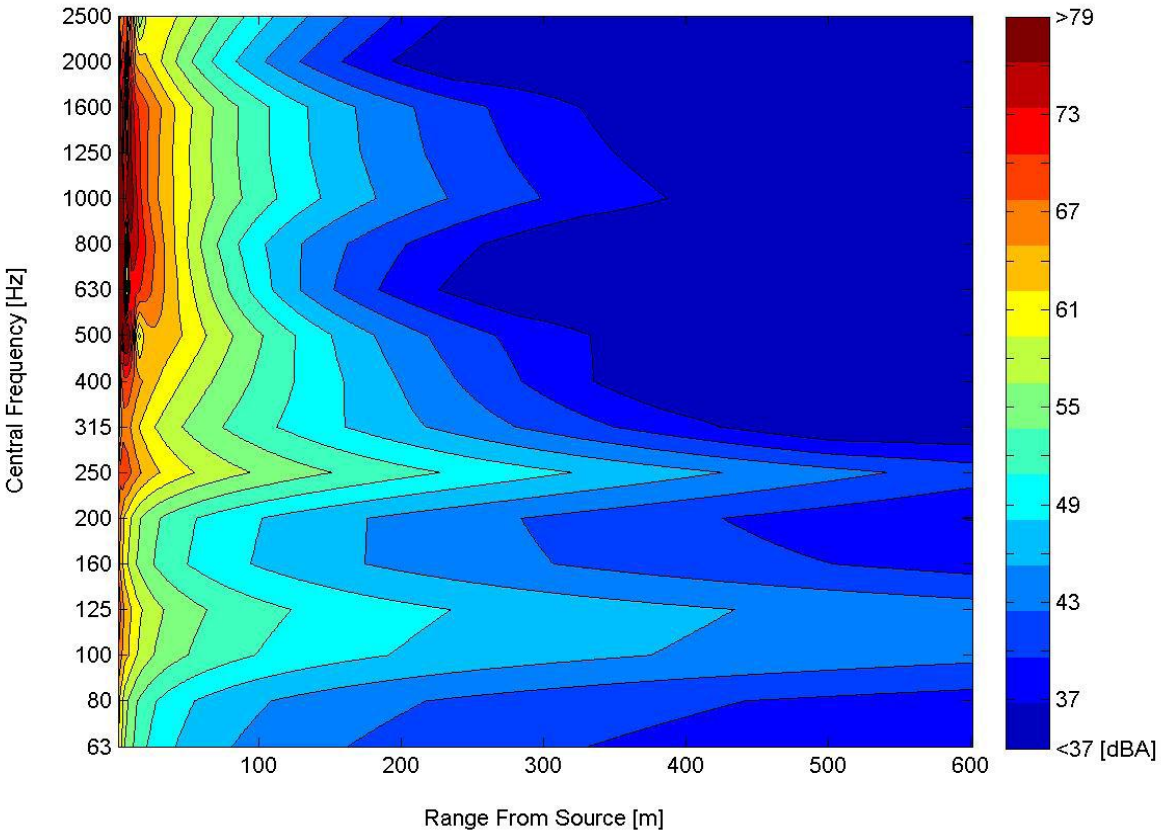

Figure 19. Spectrum vs. Range–27 Levels 3 km Grid Spacing.

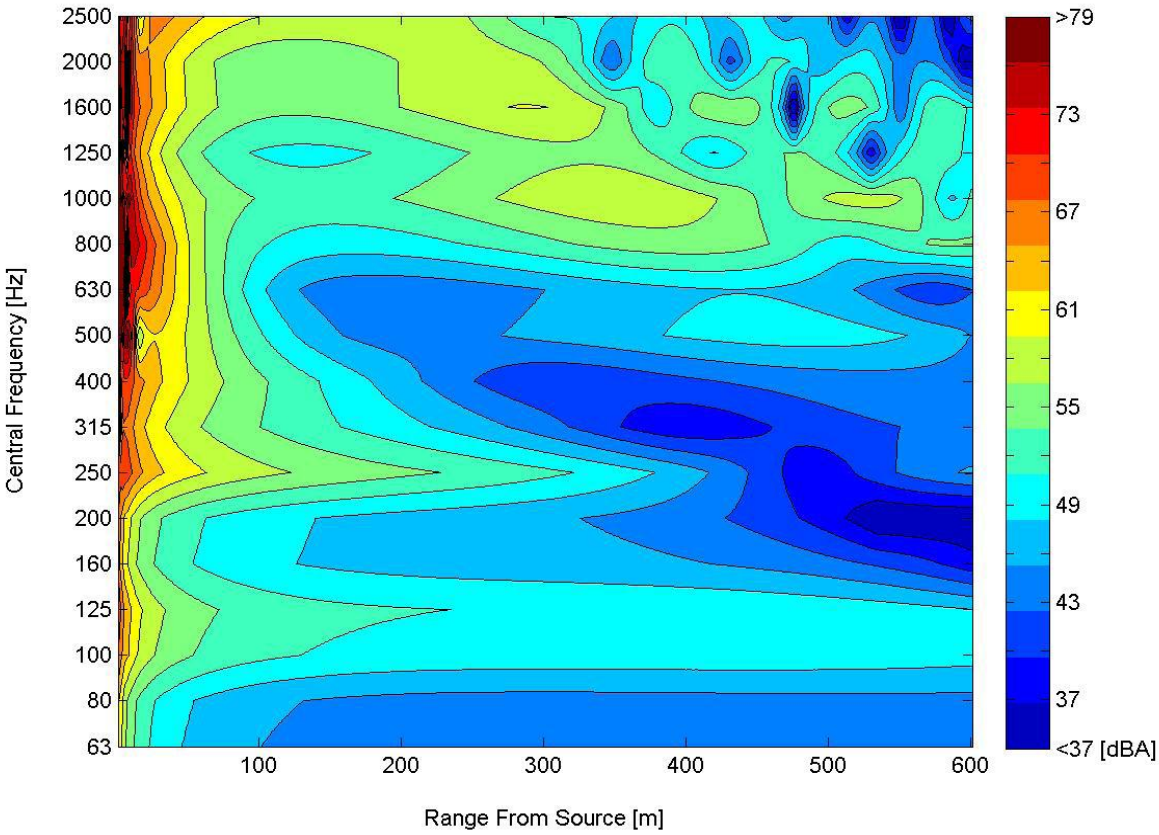

Figure 20. Spectrum vs. Range–81 Levels 1 km Grid Spacing.

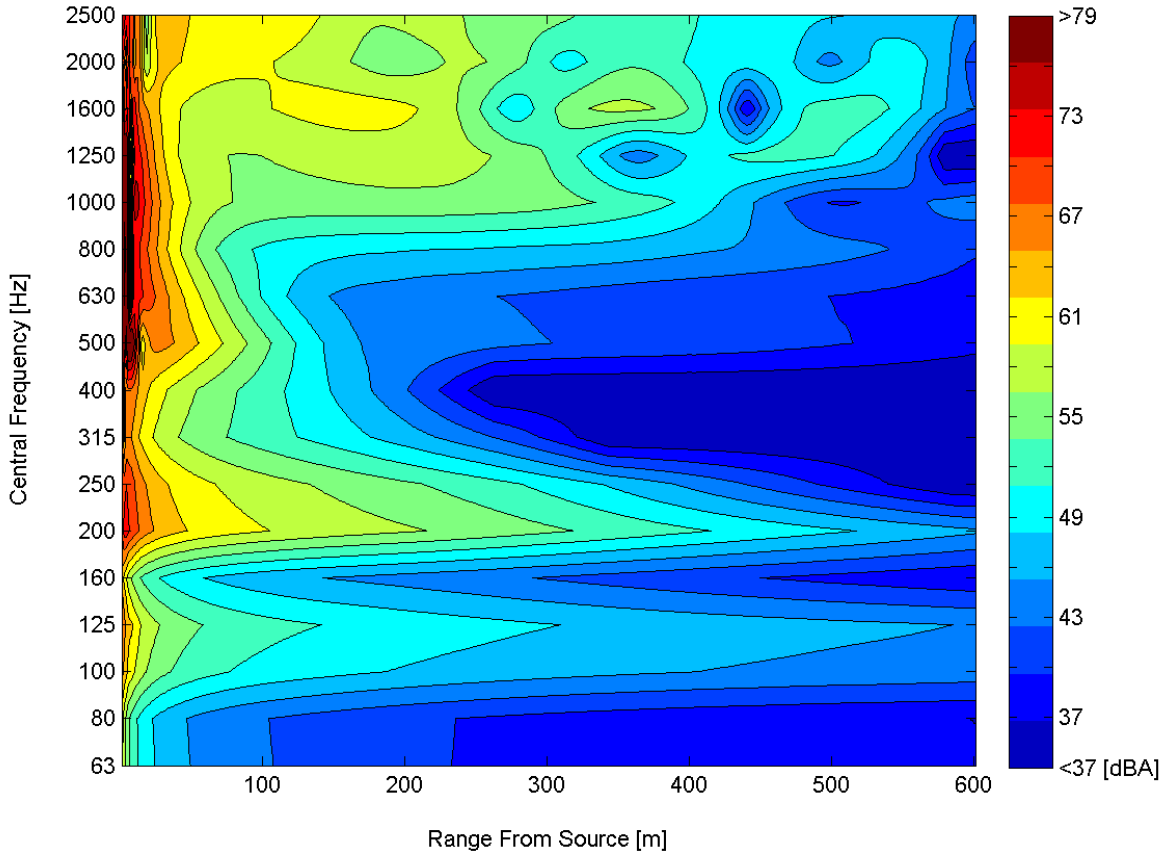

Figure 21. Spectrum vs. Range–Case A. Reproduced from Ovenden et al. (2009).

Figure 22 shows a plot of the attenuation of total A-weighted sound field relative to 50 m in range versus range from source, at 1 m AGL. The dashed blue curve represents the neutral Case B with constant temperature and zero winds, the black curve represents 27 vertical levels on the 3x3 km horizontal grid using $\tilde{C}_{eff}$, the solid blue curve represents 81 vertical levels on the 1x1 km horizontal grid, also with $\tilde{C}_{eff}$, and the dashed teal curve is from Case A of Ovenden (2009), again with $\tilde{C}_{eff}$ for that case being used. All curves were shifted according to the differences of their respective neutral cases from Case A, removing bias between profile base temperatures.

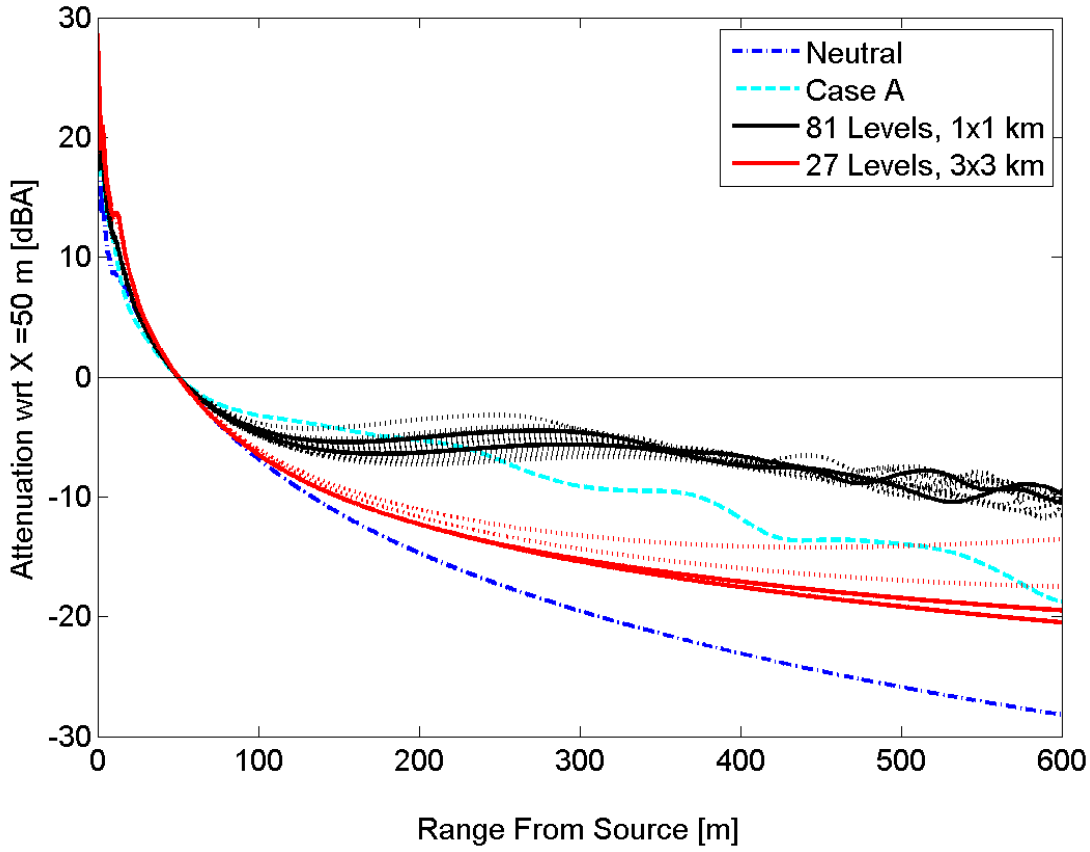

Figure 22. Attenuation vs. Range.

III.C. DISCUSSION AND CONCLUSIONS

For purposes of comparison, Appendix C includes the effective sound speed profiles and attenuation versus range plots from Ovenden et al. (2009).[5] In Figure 22, an approximately 10 dBA difference in attenuation of the total sound field is quite apparent, beginning around 100 m in range between the higher-resolution and low-resolution WRF simulations. Further, the input profile from the 27 vertical-level WRF simulation, though different from the neutral case indicating some refractive effects, is still not as significant as for the 81 vertical levels. Neither distribution of attenuation has the same form as Case A, which can be explained by the different times the profiles were taken and the effective resolution of the near-ground profile between them. The important point is the difference between the results with the two WRF model resolutions; in particular, in the higher-resolution run the vertical gradient of the effective sound speed captures the nature of the low-level shear flow and the slight temperature variations near the surface, not seen in the lower resolution run. Additionally, note that some of these measured profile details from Ovenden et al. (2009) could be due to bottom boundary conditions not realized in the 1 km x 1 km grid used in the WRF model. For instance, details of the flow due to terrain and land-use classification at levels unresolved by the 1 km grid are not present, but they could lead to a closer representation of the actual measured profile if they were accounted for. Without higher-resolution surface boundary data, it is not reasonable to increase the resolution of the WRF domain, so parameterizations need to be explored. Additionally, note that the results from WRF are for instantaneous profiles, not time-averaged profiles.

In Figures 18 and 19, the case with 27 vertical levels is not too unlike a neutral or limited refracting atmosphere, as expected from the nearly zero to slightly negative vertical gradient of the effective sound speed in Figure 17. The frequencies above 400 to 1000 Hz are suppressed in Figure 19 compared to the neutral case, indicating that either upward refraction or atmospheric absorption is responsible. Meanwhile the lower frequencies, especially around 100 Hz, are enhanced. Lower frequencies have a larger primary interference lobe near the ground (see Appendix A-4). Further, the response curve of atmospheric absorption increases nonlinearly with frequency. Therefore, lower absorption, combined with the horizontal transect's being within a larger lobe of relatively higher SPL, can explain why the lower frequencies are enhanced while the higher frequencies are suppressed compared to the neutral case.

Next, we examine the case with 81 vertical levels in Figure 20 in comparison to the neutral case. It is immediately apparent that downward refraction is taking place, especially increasing the levels of the 800 and 1000 Hz bands significantly out to 600 m range. A similar phenomenon is seen, and with similar intensities of SPL, in both Cases A and B (not reproduced) of Ovenden et al. (2009) when the vertical gradient of C_{eff} is positive. The additional features in the observational profile near the ground for Case B, as explained in Ovenden et al. (2009), cause upward refraction, giving rise to a relatively quiet zone around the 300 m range in Figure C.2 before coming back to levels comparable to 50 m in range. These details in the profiles are

[5] Refer to this publication for profiles of T and V.

likely due to local terrain features not represented in the 1 km WRF grid. Although profiles representative of inversions and jet-like features are present, and do produce significant differences between the 81-vertical-level nest compared to 27 levels, more realistic profiles are still needed to reproduce the sound field generated by the observed profiles at mid-range. Increased sound levels near the 600 m range for bands near 1000 Hz are present, however, though not as enhanced, likely because the gradient of C_{eff} is different.

In summary, we have shown that conditions of morning temperature inversion and low-level jet or wind shear can be reasonably reproduced using WRF with increased vertical levels. The computational effort required to obtain the higher resolution is greatly reduced by utilizing vertical nesting. Further, these profiles can be used to generate sound fields representative of observations during morning conditions. However, more detailed structures of the profiles are still needed, requiring higher-resolution information about the terrain or some form of sub-grid parameterization scheme.

III.D. FUTURE WORK

First, the coupled models should be run for times corresponding to the exact observed times, not just similar morning conditions. However, one must keep in mind not only the observational uncertainties, but the difference between the time-averaged and instantaneous values being compared. Considering that the WRF model is downscaled from global atmospheric model data output every 6 hours with 100 km horizontal spacing to obtain less than 20 m near-ground vertical resolution on a 1 km horizontal grid, representative profiles are quite suitable for use in conjunction with the sound model. Furthermore, because the WRF model is an exact physics-based solver, the sensitivities of high-resolution near-ground profiles to model configurations should be explored. For instance, various PBL and urban physics schemes should be explored to see whether significant effects on flow details are observed and to determine whether an optimal combination of schemes exists for the particular case of resolving near-ground flow details in the Phoenix region. Resolution and sub-grid parameterizations become increasingly important when moving to domains with more complex urban canopies (Fernando et al. 2010). Capturing such details within WRF and coupling WRF to an acoustic model is certainly a main focus of future explorations, especially in conjunction with terrain-following acoustic models.

IV. FUTURE POSSIBILITIES

Future work to increase resolution to at least 100 m should be attempted using either the national land cover database (NLCD) (Vogelmann et al. 2001; Homer et al. 2007), where land use up to 90 m resolution is available within the conterminous United States (CONUS) region, or the Shuttle Radar Topography Mission (SRTM) (Farr et al. 2007) which features topographical data available at 30 m resolution globally. These higher-resolution ground boundary data would enable higher-resolution horizontal nesting, which would in turn make finer vertical-resolution nesting. Additionally, effects on the near-ground profiles due to the various PBL and land surface model (LSM) schemes could be explored at this higher resolution. Running WRF in a large eddy simulation (LES) mode could also resolve turbulent features at scales important to modeling of sound propagation, observed as fluctuations in sound level from a constant source at a fixed receiver position. Furthermore, these profiles derived with WRF could be used to feed a computational fluid dynamics model such as FLUENT to account for flow response to artificial terrain features such as walls and trees, effects of which already have significant results on acoustics (Raupach and Thom 1981; Salomons 1999; Heimann 2003a; Heinmann 2003b; van Renterghem et al. 2005, 2007, 2008, 2010; Bucur 2006; Heimann and Karle 2006; Aballea and Defrance 2004).[6] The typical model is either a finite difference time domain simulation, which is significantly more computationally expensive but is capable of exact three-dimensional complications, or a simple ray-based model that leaves out some potentially important atmospheric effects. Boundary element models are also quite common, though not discussed in this report.

Profiles obtained from WRF forecasting within a high-resolution nest could be used as input conditions for a higher-resolution computational fluid dynamics simulation of flow over terrain features (berms and walls, trees and neighborhoods), the output of which could then feed a GTPE model by treating the effective sound speed as a 2D scalar rather than a 1D profile. Optimal mitigation strategies could then be identified based upon a set of terrain configurations adjacent to sources and a set of meteorological conditions expected for given regions at times when problematic sources are expected to be present.

Parameterizations of highway source strength and position in terms of remotely observable factors (e.g., via existing networks of camera and radar systems) such as vehicle composition, number density, and velocity at different times of the day and along different road segments, as together with the ability to forecast meteorological profiles of sufficient resolution on a large scale (e.g., by using WRF) would provide important improvements to modeling inputs. Such improved inputs to an acoustic model like GTPE, which can account for terrain and reflections, may enable noise studies conducted at a single site to be upscaled to the entire Phoenix Valley or other regions of interest. Locations of particularly excessive noise could then be assessed to guide mitigation. Field measurements of comparable magnitude have been performed, for instance in Taiwan (Tsai et al. 2009); Chile (Sommerhoff 2004); Paris, France (Butler 2004); Madrid, Spain (Manvell et al. 2004); and other locations. Models currently exist

[6] Note that none of these studies used the GTPE model with backscatter that we have developed.

(King and Rice 2009; Manvell et al. 2004; Reiter et al. 2008) that perform such estimates, but they either neglect the full profile of the meteorological fields or simply use Pasquill atmospheric stability classes (Sutherland et al. 1986; Pasquill 1961; Smith 1979) for the entire study region. Hence, they do not capture the detailed structures of the medium through which the sound waves are propagating or the detailed spatial variability of the meteorological profiles that would be present in a well-developed urban/sub-urban area, especially in settings with complex terrain (Fernando et al. 2010). As such, these models could be a good baseline for comparison with neutral or simplified conditions, where only ground-level temperature or conditions appropriate for the specific classes are considered, and thus could provide benchmarks for performance of more detailed models.

Additionally, effects of future land-use changes and regional climate modifications on near-ground meteorological profiles could also be explored and coupled to a noise propagation model utilizing an acoustic source parameterization scheme. Acoustic source modeling could incorporate aspects such as estimates of future traffic loads, vehicle types, and speed, on roadway segments. Such a model would need to consider future vehicle characteristics which are acoustically relevant, and quite vehicle type dependent, with engine-, tire-, and body-generated aeroacoustic noise, being three main examples. Furthermore, the propagation model is not limited specifically to highway noise, and near-field coupling for different acoustic sources could be applied. This will allow investigations of the change of soundscape with future growth of both the metropolitan area and the transportation infrastructure.

For any prognostic model, comprehensive validation testing or comparison with benchmark cases should be performed. In terms of an acoustic model, this validation would be made by placing receivers at key locations within the domain where simulated noise levels have strong sensitivity to the model parameters (e.g., source, boundary, and medium/meteorological characteristics). Since the cost associated with a large array of microphones is prohibitive, the model could be run in advance under a set of expected conditions to guide the placement of additional microphones for the purpose of model validation for specific terrain cases that may not have benchmark comparisons.

V. CONCLUSIONS/FURTHER COMMENTS

(i) A Generalized Terrain Parabolic Equation (GTPE) model, following the work of Sack and West (1995), was developed to describe sound propagation in varying terrain. The GTPE model was extended by deriving a reflection scheme based on the normal impedance ground boundary condition to account for two-way propagation. Thus, our new model enables the study of backscatter from vertical terrain features, in addition to forward propagation of traffic noise in settings with complex terrain. Some results for simplified terrain cases without meteorological effects were presented to illustrate the capabilities of the new model and the effects of terrain in a neutral atmosphere.

(ii) The new option of vertical nesting implemented in ARW-WRF v3.2 within the finest nest was used to amalgamate meteorological effects with the highway noise pollution model of Ovenden et al. (2009), which was applied to the Phoenix metropolitan area. Vertical profiles were extracted from model runs with near-ground resolution finer than 20 m, to provide input into a sound propagation model and produce forecasts of noise pollution from a highway line segment noise source. The vertical nesting improved the resolution of finer structures of the temperature and velocity profiles, such as temperature inversions and low-level, jet-like features.

(iii) The model accounts for terrain obstacles via a complex impedance value, with the transmitted field being set to zero (perturbed) complex pressure. To handle facades of walls or buildings, the model grid needs to first resolve such features, upon which the extension of the vertical wall reflection to nearly vertical or arbitrary angles can be explored. An alternate approach would be to utilize nested sub-regions within the PE domain.

(iv) The results of the modeling system combining WRF and Ovenden et al. (2009) appear to be physically and intuitively sound, although detailed model verifications were not performed because of the inadequacy of available data. The improvements gained by using GTPE for moderate terrain and with reverberations over calculations with flat-terrain and simplified analytic approximations are yet to be determined; this area is recommended for future research. To this end, data taken with an array of microphones will be needed. The placement of extra microphones could be determined for each terrain configuration to optimize results for distinguishing among the influences of different meteorological cases.

(v) The urban landscape is complex; so, too, is the urban soundscape due to intricate flow patterns, stratification conditions, and acoustic reflections. Special (most often commercial) software will be needed to handle micrometeorology in urban cases and should be coupled with an acoustic model. Simplifications are also possible; for

example, (e.g., Pasquill) stability classes and software built upon ray-based models could be used. The predictions of such techniques should be compared with PE/GTPE models.

(vi) Future model developments should extend the current reflection scheme to terrain features with arbitrary angles. Future possibilities include coupling of the sound model with flow calculation software to determine the flow response to terrain and the sound field response to perturbed flow.

REFERENCES

Aballea, F-E. and J. Defrance. 2004. “Single and Multiple Reflections in Plane Obstacle Using the Parabolic Equation Method with a Complementary Kirchhoff Approximation.” In *Proc 7eme Congres Francais d'Acoustique, Strasbourg, France.*

Attenborough, K., K. M. Li, and K. Horoshenkov. 2007. *Predicting Outdoor Sound.* New York: Taylor & Francis Group.

Bowman, J. J., T. B. A. Senior, and P. L. E. Uslenghi. 1987. *Electromagnetic and Acoustic Scattering by Simple Shapes*. Revised Printing. New York: Hemisphere Publishing Corporation.

Bucur, V. 2006. *Urban Forest Acoustics*. Berlin: Springer Verlag.

Butler, D. 2004. “Noise Management: Sound and Vision.” *Nature* 427: 480-481, 5 February.

Delany, M. E. and E. N. Bazley. 1970. “Acoustical Properties of Fibrous Absorbent Materials.” *Applied Acoustics* 3 (2): 105–116, April.

Farr, T. G., P. A. Rosen, E. Caro, R. Crippen, R. Duren, S. Hensley, M. Kobrick, M. Paller, E. Rodriguez, L. Roth, D. Seal, S. Shaffer, J. Shimada, J. Umland, M. Werner, M. Oskin, D. Burbank, and D. Alsdorf. 2007. “The Shuttle Radar Topography Mission.” *Reviews of Geophysics* 45 (2), RG2004. doi:10.1029/2005RG000183, May.

Fernando, H. J. S., D. Zajic, S. Di Sabatino, R. Dimitrova, B. Hedquist. and A. Dallman. 2010. “Flow, Turbulence, and Pollutant Dispersion in Urban Atmospheres.” *Physics of Fluids* 22 (5), 051301/20.

Forman, R. T. T. and R. D. Deblinger. 2000. “The Ecological Road-Effect Zone of a Massachusetts (U.S.A.) Suburban Highway.” *Conservation Biology* 14 (1): 36-46, February.

Gauvreau, B., M. Bérengier, P. Blanc-Benon, and C. Depollier. 2002. “Traffic Noise Prediction with the Parabolic Equation Method: Validation of a Split-Step Pade Approach in Complex Environments.” *Journal of the Acoustical Society of America* 112 (6): 2680-2687, December.

Hatch, L., C. Clark, R. Merrick, S. van Parijs, D. Ponirakis, K. Schwehr, M. Thompson, and D. Wiley. 2008. “Characterizing the Relative Contributions of Large Vessels to Total Ocean Noise Fields: A Case Study Using the Gerry E. Studds Stellwagen Bank National Marine Sanctuary.” *Environmental Management* 42 (5): 735-752, November.

Heimann, D. 2003a. “Meteorological Aspects in Modeling Noise Propagation Outdoors.” *Proceedings of Euronoise Naples 2003* paper ID:213-IP.

Heimann, D. 2003b. “Numerical Simulations of Wind and Sound Propagation Through an Idealized Stand of Trees.” *Acta Acustica united with Acustica* 89 (5): 779-788, September/October.

Heimann, D. and R. Karle. 2006. “A Linearised Euler Finite-Difference Time-Domain Sound Propagation Model with Terrain-Following Coordinates.” *Journal of the Acoustical Society of America* 119 (6): 3813-3821.

Homer, C., J. Dewitz, J. Fry, M. Coan, N. Hossain, C. Larson, N. Herold, A. McKerrow, J. N. VanDriel, and J. Wickham. 2007. “Completion of the 2001 National Land Cover Database for the Conterminous United States.” *Photogrammetric Engineering & Remote Sensing* 73 (4): 337-341, April.

King, E. A. and H. J. Rice. 2009. “The Development of a Practical Framework for Strategic Noise Mapping.” *Applied Acoustics* 70 (8): 1116-1127, August.

Li, Y. L., S. J. Franke, and C. H. Liu. 1993. “Wave Scattering from a Ground with a Gaussian Bump or Trough in an Inhomogeneous Medium.” *Journal of the Acoustical Society of America* 94 (2): 1067-1075, August.

Mahalov, A. and M. Moustaoui. 2009. “Vertically Nested Nonhydrostatic Model for Multiscale Resolution of Flows in the Upper Troposphere and Lower Stratosphere.” *Journal of Computational Physics* 228 (4): 1294-1311, March.

Manvell, D., L. B. Marcos, H. Stapelfeldt, and R. Sanz. 2004. “SADMAM – Combining Measurements and Calculations to Map Noise in Madrid.” Inter-Noise 2004, The 33rd International Congress and Exposition On Noise Control Engineering, Prague, Czech Republic, August 22-25.

Moudon, A. V. 2009. “Real Noise from the Urban Environment: How Ambient Community Noise Affects Health and What Can Be Done About It.” *American Journal of Preventive Medicine* 37 (2): 167-171, August.

National Centers for Environmental Prediction, National Weather Service, NOAA, U.S. Department of Commerce. 2000, updated daily. “NCEP FNL Operational Model Global Tropospheric Analyses, continuing from July 1999, [dataset] ds083.2.” Research Data Archive at the National Center for Atmospheric Research, Computational and Information Systems Laboratory. http://rda.ucar.edu/datasets/ds083.2.

Nelson, J. P. 1982. “Highway Noise and Property Values: A Survey of Recent Evidence.” *Journal of Transport Economics and Policy* 16 (2): 117-138, May.

Ovenden, N., S. Shaffer, S., and H. Fernando. 2009. “Impact of Meteorological Conditions on Noise Propagation from Freeway Corridors.” *Journal of the Acoustical Society of America* 126 (1): 25-35.

Pasquill, F. 1961. “The Estimation of the Dispersion of Windborne Material.” *Meteorological Magazine* 90: 33-49.

Passchier-Vermeer, W. and W. F. Passchier. 2000. “Noise Exposure and Public Health.” *Environmental Health Perspectives* 108 (suppl. 1): 123-131, March.

Rasmussen, K. 1985. “On the Effect of Terrain Profile on Sound Propagation Outdoors.” *Journal of Sound and Vibration* 98 (1): 35-44, January.

Raupach, M. R. and A. S. Thom. 1981. “Turbulence In and Above Plant Canopies.” *Annual Reviews of Fluid Mechanics* 13: 97-129, January.

Reiter, M., J. Kotus, and A. Czyzewski. 2008. “Optimizing Localization of Noise Monitoring Stations for the Purpose of Inverse Engineering Applications.” *Acoustics 2008,* Paris, France, June 29-July 4, 253-258.

Rheindt, F. E. 2003. “The Impact of Roads on Birds: Does Song Frequency Play a Role in Determining Susceptibility to Noise Pollution?” *Journal of Ornithology* 144 (3): 295-306, July.

Robertson, J. S. 1999. “Sound Propagation over a Large Wedge: A Comparison Between the Geometrical Theory of Diffraction and the Parabolic Equation.” *Journal of the Acoustical Society of America* 106 (1): 113-119.

Sack, R. A. and M. West. 1995. “A Parabolic Equation for Sound Propagation in Two Dimensions Over Any Smooth Terrain Profile: The Generalized Terrain Parabolic Equation (GT-PE).” *Applied Acoustics* 45 (2): 113-129.

Salomons, E. M. 1999. “Reduction of the Performance of a Noise Screen Due to Screen-Induced Wind-Speed Gradients. Numerical Computations and Wind Tunnel Experiments.” *Journal of the Acoustical Society of America* 105 (4): 2287–2293.

Salomons, E. M. 2001. *Computational Atmospheric Acoustics*. Norwell, Massachusetts: Kluwer Academic Publishers.

Skamarock, W. C. and J. B. Klemp. 2008. “A Time-Split Nonhydrostatic Atmospheric Model for Weather Research and Forecasting Applications.” *Journal of Computational Physics* 227 (7): 3465-3485, March.

Skamarock, W. C., J. B. Klemp, J. Dudhia, D. O. Gill, D. M. Barker, M. G. Duda, X.-Y. Huang, W. Wang, and J. G. Powers. 2008. "A Description of the Advanced Research WRF Version 3." National Center for Atmospheric Research Technical Note NCAR/TN-475+STR, June, 113 pgs.

Smith, F. B. 1979. "The Relation Between Pasquill Stability *P* and Kazanski-Monin Stability μ (In Neutral and Unstable Conditions)." *Atmospheric Environment* 13 (6): 879-881.

Sommerhoff, J., M. Recuero, and E. Suárez. 2004. "Community Noise Survey of the City of Valdivia, Chile." *Applied Acoustics* 65 (7): 643-656, July.

Stull, R. B. 1988. *An Introduction to Boundary Layer Meteorology*. Norwell, Massachusetts: Kluwer Academic Publishers.

Sutherland, R. A., F. V. Hansen, and W. D. Bach. 1986. "A Quantitative Method for Estimating Pasquill Stability Class from Windspeed and Sensible Heat Flux Density." *Boundary-Layer Meteorology* 37 (4): 357-369, December.

Tsai, K.-T., M.-D. Lin, and Y.-H. Chen. 2009. "Noise Mapping in Urban Environments: A Taiwan Study." *Applied Acoustics* 70 (7): 964-972.

Van Renterghem T., E. M. Salomons, and D. Botteldooren. 2005. "Efficient FDTD-PE Model for Sound Propagation in Situations with Complex Obstacles and Wind Profiles." *Acta Acustica united with Acustica* 91 (4): 671-679, July/August.

Van Renterghem, T., D. Botteldooren, and P. Lercher. 2007. "Comparison of Measurements and Predictions of Sound Propagation in a Valley-Slope Configuration in an Inhomogeneous Atmosphere." *Journal of the Acoustical Society of America* 121 (5): 2522-2533, May.

Van Renterghem, T. and D. Botteldooren. 2008. "Numerical Evaluation of Tree Canopy Shape Near Noise Barriers to Improve Downwind Shielding." *Journal of the Acoustical Society of America* 123 (2): 648-657, February.

Van Renterghem, T. and D. Bottledooren. 2010. "Meteorological Influence on Sound Propagation Between Adjacent City Canyons: A Real-Life Experiment." *Journal of the Acoustical Society of America* 127 (6): 3335-3346.

Vogelmann, J. E., S. M. Howard, L. Yang, C. R. Larson, B. K. Wylie, and N. Van Driel. 2001. "Completion of the 1990s National Land Cover Data Set for the Conterminous United States from Landsat Thematic Mapper Data and Ancillary Data Sources." *Photogrammetric Engineering & Remote Sensing* 67: 650-662, June.

APPENDIX A. GTPE MODEL DERIVATION KEY STEPS

Splitting the second order hyperbolic operator Q_{eff}^2 in Equation A.1 into a parabolic model Equation A.2 depends upon the commutator in Equation A.3 of the operator Q_{eff} with the derivative in the propagation direction ∂_xbeing zero:

$$\left(\partial_{xx} + k^2 Q_{eff}^2\right)p = 0, \quad \text{(Eq. A.1)}$$

$$\left(\partial_x + ikQ_{eff}\right)\left(\partial_x - ikQ_{eff}\right)p = 0, \quad \text{(Eq. A.2)}$$

$$\left[\partial_x, Q_{eff}(x)\right] \neq 0, \quad \text{(Eq. A.3)}$$

where the relation in Equation A.3 holds if Q_{eff} depends upon *x*, which is true for the general Helmholtz equation with the terrain transformation in Equation A.4.

$$\left[\partial_{\xi\xi} - 2H'^{\partial_{\xi\eta}} - H''^{\partial_\eta} + \left(H'^2 + 1\right)\partial_{\eta\eta} + k^2\right]\psi = 0, \quad \text{(Eq. A.4)}$$

Following the derivation in Sack and West 1995, the GTPE model Equation A.4 can be presented as

$$\left[\frac{i}{2k_0} L_1[\varphi] + 2ik_0\varphi - 2H'\partial_\eta\varphi\right]_a^b + \int_a^b \alpha(\xi')\partial_{\eta\eta}\varphi d\xi' + \int_a^b \chi(\xi')\partial_\eta\varphi d\xi' + \int_a^b \gamma(\xi', \eta)\varphi d\xi' = 0 \quad \text{(Eq. A.5)}$$

where the functions α,β and χ represent the terrain transformation, and γ accounts for the medium by variations of the wavenumber *k* with respect to a reference wavenumber k_0. The integration is over a range step in the interval (a,b), and the integrals are numerically approximated with trapezoidal representations of Equation A.6 as

$$\int_a^b \kappa(\xi')\partial_{\eta^n}\varphi(\xi')d\xi' \approx A_\kappa\partial_{\eta^n}\varphi(a) + B_\kappa\partial_{\eta^n}\varphi(b) \quad \text{(Eq. A.6)}$$

With

$$A_\kappa = \Delta_\xi\left(\frac{\kappa(a)}{3} + \frac{\kappa(b)}{6}\right)$$

$$B_\kappa = \Delta_\xi\left(\frac{\kappa(a)}{6} + \frac{\kappa(b)}{3}\right)$$

Where $\kappa=\alpha, \beta, \gamma$ or χ and $n=0,1,2$ is the order of the derivative.

When using the discrete first and second derivative operators,

$$\delta = \begin{bmatrix} 0 & 1 & & & \\ -1 & 0 & 1 & & \\ & \ddots & \ddots & \ddots & \\ & & \ddots & \ddots & 1 \\ & & & -1 & 0 \end{bmatrix} \qquad \delta^2 = \begin{bmatrix} -2 & 1 & & & \\ 1 & -2 & 1 & & \\ & \ddots & \ddots & \ddots & \\ & & \ddots & \ddots & 1 \\ & & & 1 & -2 \end{bmatrix} \qquad \text{(Eq. A.7)}$$

yielding the matrix equation $M\varphi(a)=N\,\varphi(a)$, which can be written using A.1.6 and A.1.7 in A.1.5 as

$$\underbrace{\begin{bmatrix} \frac{1}{\Delta_\eta^2}\left(\frac{i}{2k_0}\alpha(b)+B_\alpha\right)\delta^2 + \\ \frac{-1}{\Delta_\eta}\left(\frac{i}{2k_0}\beta(b)+2H'(b)-B_\chi\right)\delta + \\ \left(\frac{i}{2k_0}\gamma(b)+B_\gamma+2ik_0\right) \end{bmatrix}}_{M} \varphi(b) = \underbrace{\begin{bmatrix} \frac{1}{\Delta_\eta^2}\left(\frac{i}{2k_0}\alpha(a)-A_\alpha\right)\delta^2 + \\ \frac{-1}{\Delta_\eta}\left(\frac{i}{2k_0}\beta(a)+2H'(a)+A_\chi\right)\delta + \\ \left(\frac{i}{2k_0}\gamma(a)-A_\gamma+2ik_0\right) \end{bmatrix}}_{N} \varphi(a) \qquad \text{(Eq. A.8)}$$

The general domain decomposition used for the GTPE model is shown in Figure A.1. The division between Green's function and GTPE model is made at the boundary of the asphalt to sandy soil interface. The starting pressure field at this interface is obtained by solving Green's function for a line source at height L_0 above the center of the near travel lane if asphalt is used. An absorbing buffer zone exponentially attenuates the top 100 m of the domain to prevent artificial reflections from the domain top boundary. Coordinate transformation has been made from x,z to xi, etc.

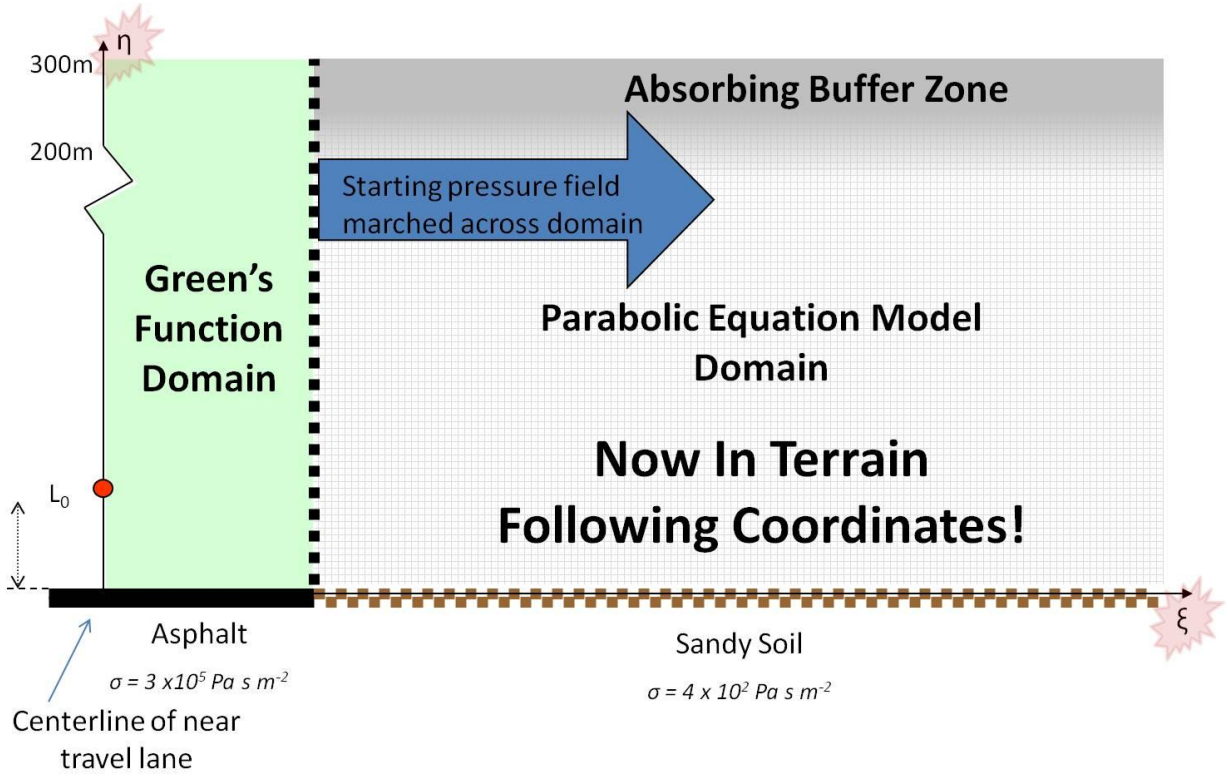

Figure A.1. GTPE Domain Configuration.

APPENDIX B. SETUP AND SUPPLEMENTARY FIGURES FROM WRF SIMULATIONS

Table B.1. Typical Physics and Dynamics Model Options from the namelist.input File for the WRF Model Simulations.

```
&physics
mp_physics                  = 3,
ra_lw_physics               = 1,
ra_sw_physics               = 1,
radt                        = 30,
sf_sfclay_physics           = 1,
sf_surface_physics          = 1,
bl_pbl_physics              = 1,
bldt                        = 0,
cu_physics                  = 1,
cudt                        = 5,
isfflx                      = 1,
ifsnow                      = 0,
icloud                      = 1,
surface_input_source        = 1,
num_soil_layers             = 5,
sf_urban_physics            = 0,
mp_zero_out                 = 0,
maxiens                     = 1,
maxens                      = 3,
maxens2                     = 3,
maxens3                     = 16,
ensdim                      = 144,
```

```
&dynamics
w_damping                   = 0,
diff_opt                    = 1,
km_opt                      = 4,
diff_6th_opt                = 0,
diff_6th_factor             = 0.12,
base_temp                   = 290.,
damp_opt                    = 0,
zdamp                       = 5000.,
dampcoef                    = 0.01,
khdif                       = 0,
kvdif                       = 0,
smdiv                       = 0.1,
emdiv                       = 0.01,
epssm                       = 0.1,
time_step_sound             = 4,
h_mom_adv_order             = 5,
v_mom_adv_order             = 3,
h_sca_adv_order             = 5,
v_sca_adv_order             = 3,
non_hydrostatic             = .true.,
moist_adv_opt               = 1,
scalar_adv_opt              = 1,
chem_adv_opt                = 1,
tke_adv_opt                 = 1,
```

Figure B.1 shows temperature profiles derived from potential temperature for the 27 vertical level 3x3 km grid (red) and the 81 vertical level 1x1 km grid (black) for the closest grid points (green) and the nearest neighbors (dashed) for the lowest 400 meters (left) and the full vertical extent of ≈ 20 km (right). Vertical levels are indicated by green squares (lowest 13 of 81) and red circles (lowest 5 of 27) in the left panel for the two profiles closest to the site.

The plots in Figures B.2 through B.4 are the same as for Figure B.1, except that Figure B.2 shows WRF profiles of potential temperature (θ); Figure B.3 shows WRF profiles of the U-component of velocity; and Figure B.4 shows WRF profiles of the W-component of velocity.

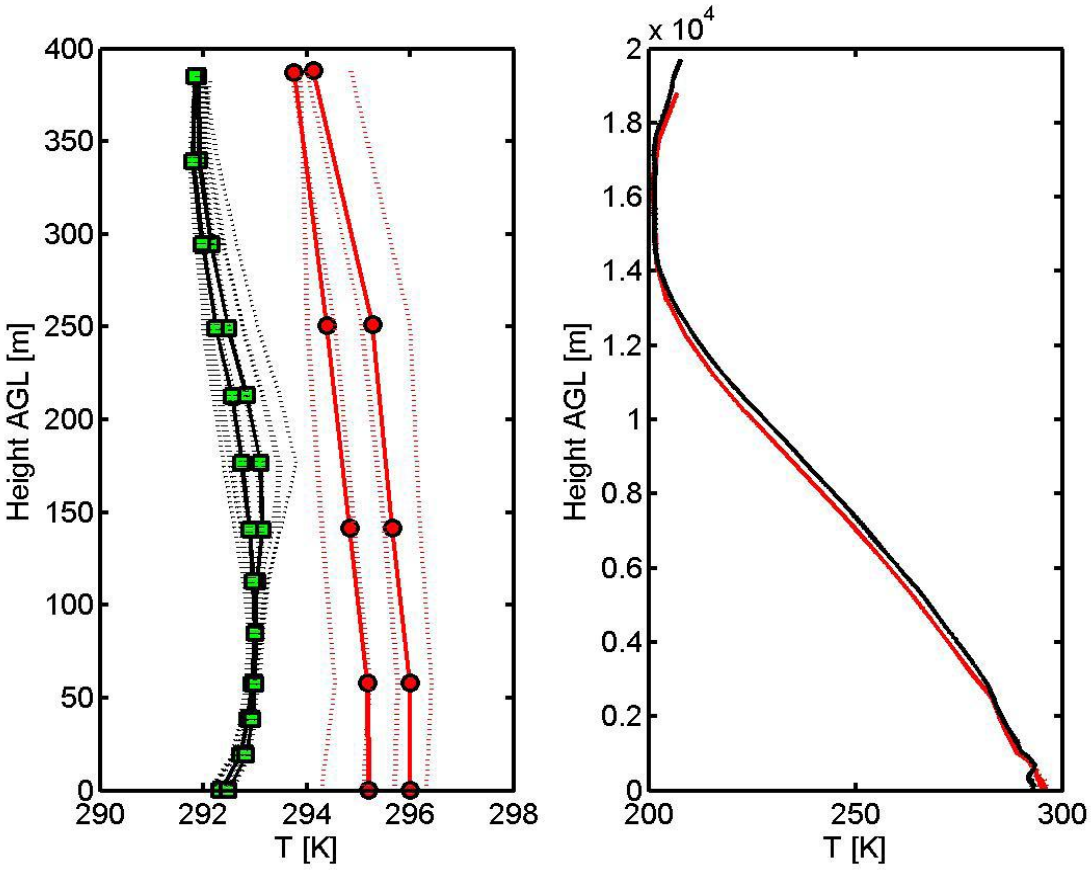

Figure B.1. WRF Profiles of Temperature.

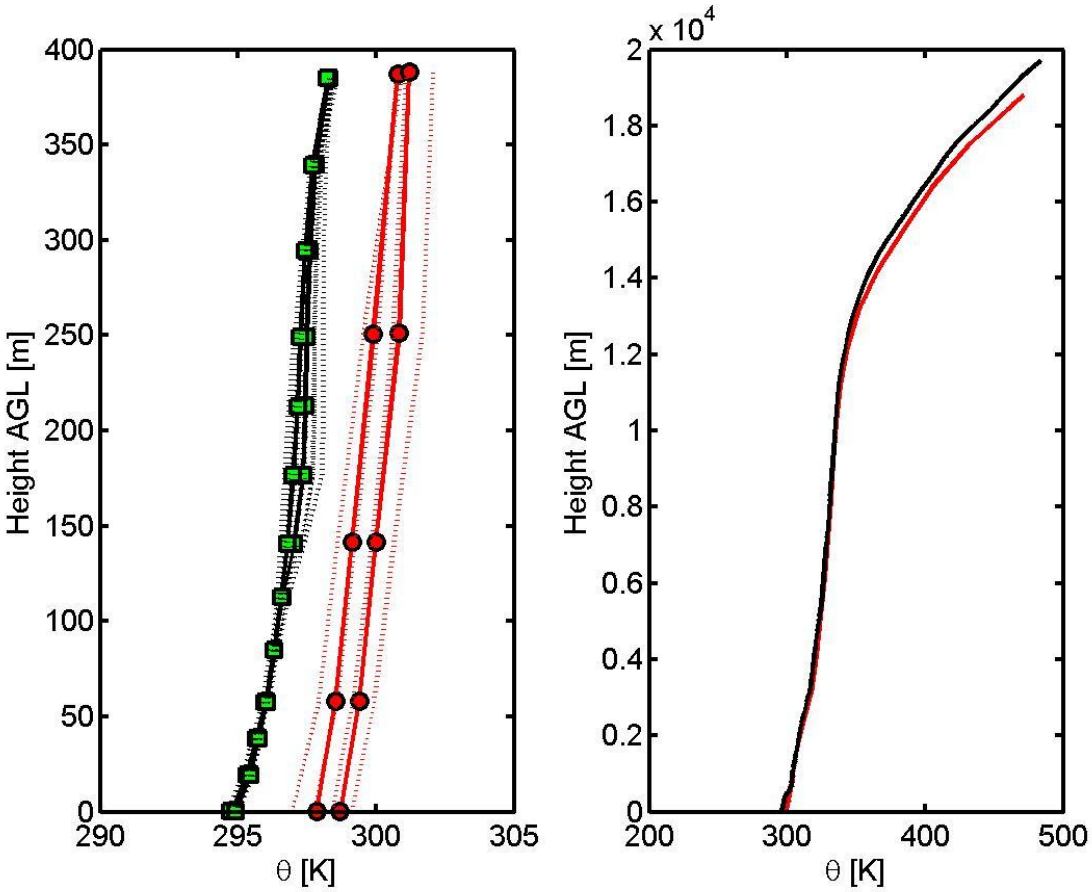

Figure B.2. WRF Profiles of Potential Temperature.

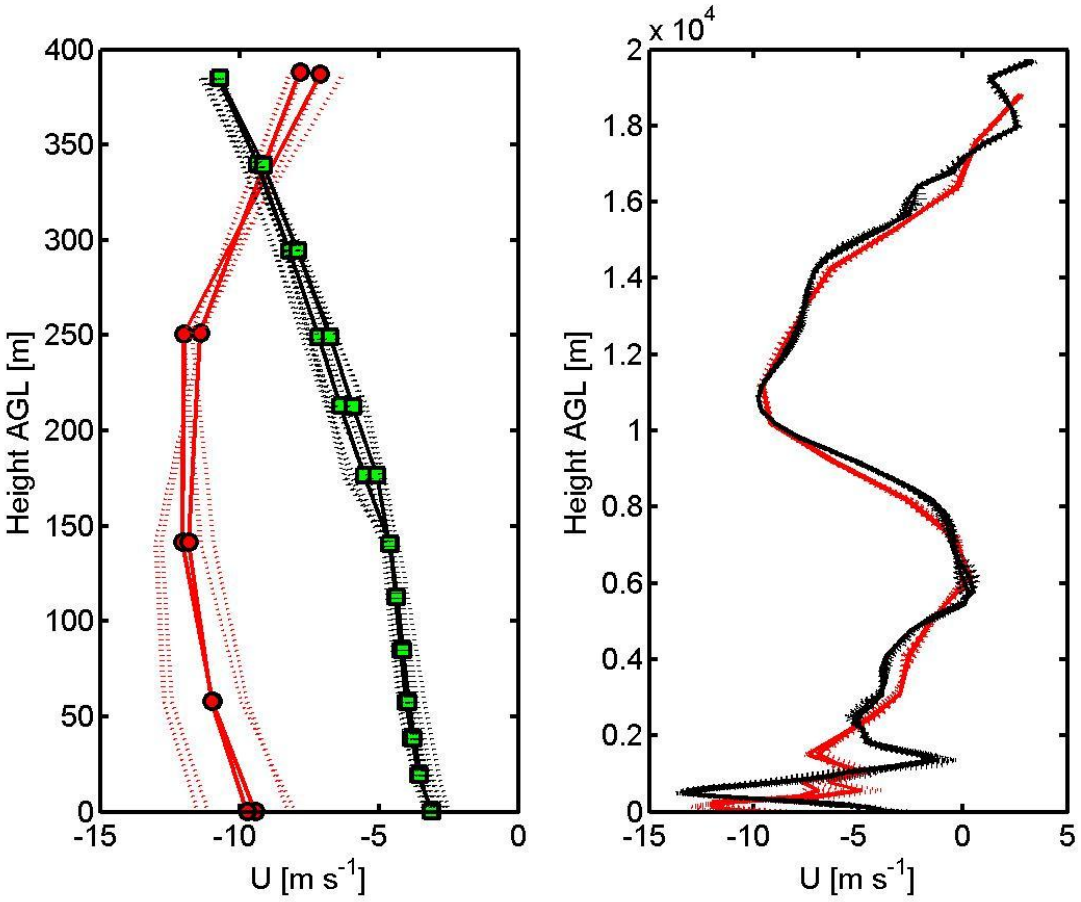

Figure B.3. WRF Profiles of U Component of Velocity.

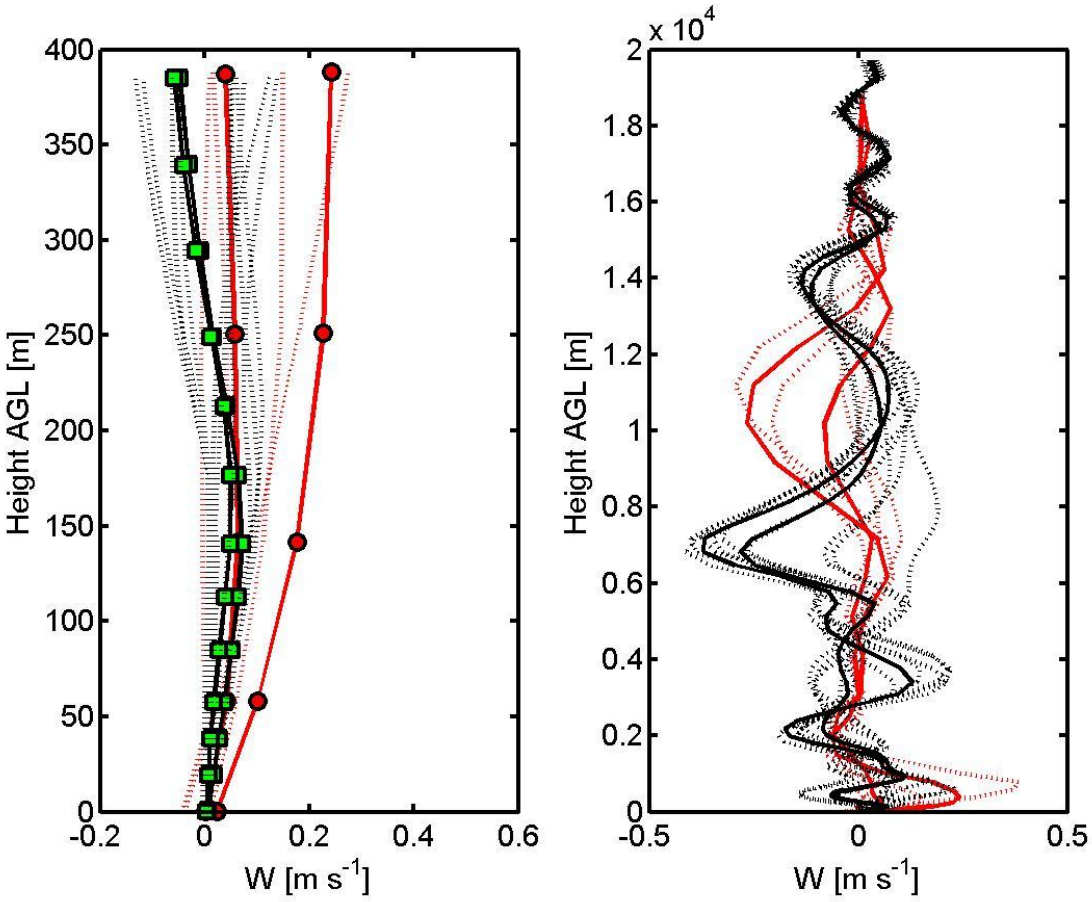

Figure B.4. WRF Profiles of W Component of Velocity.

APPENDIX C. COMPARISON DATA AND MODEL CONFIGURATION FROM OVENDEN ET AL. (2009)

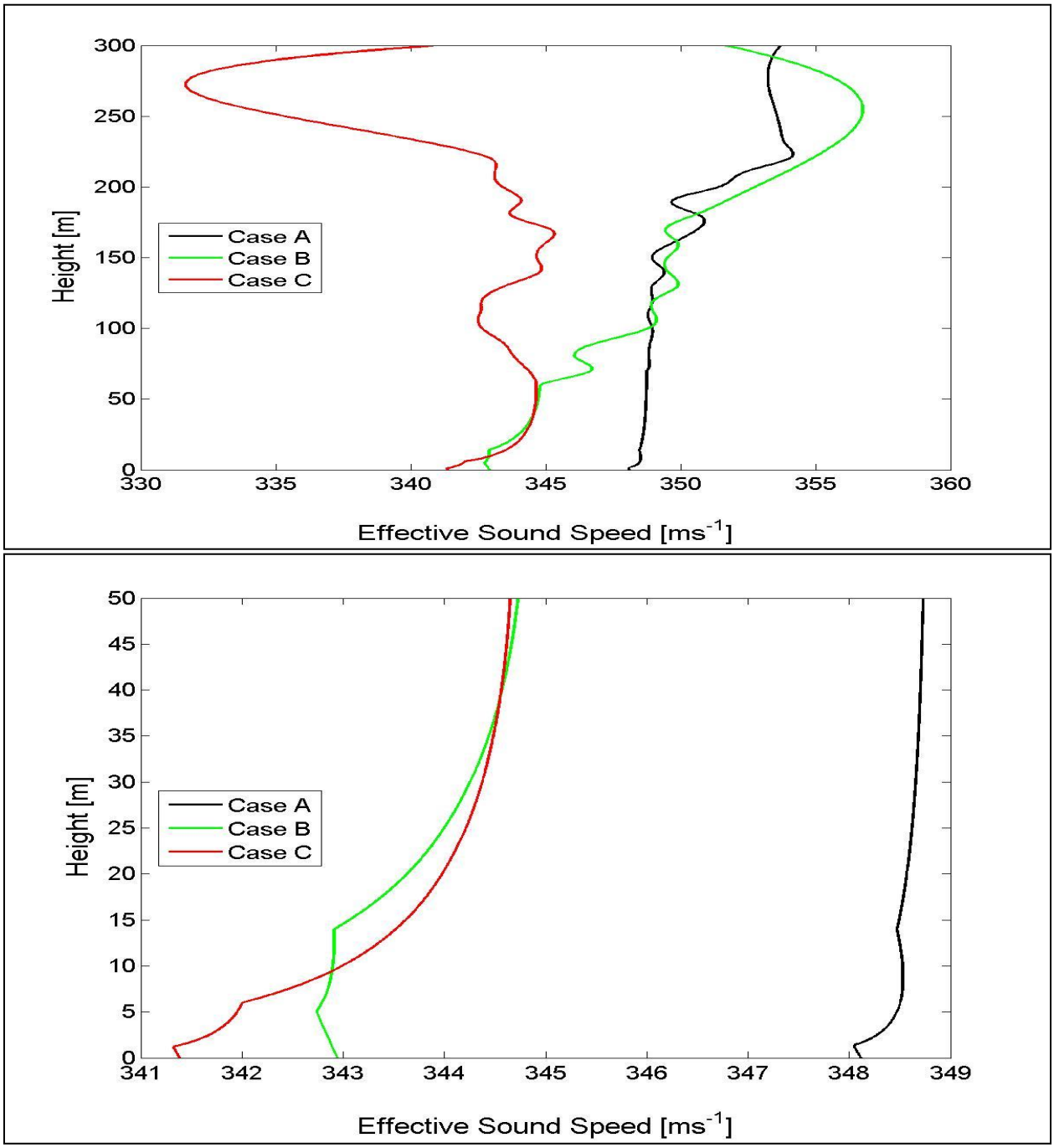

Figure C.1. Effective Sound Speed Profiles from Ovenden et al. (2009).

For comparison, the effective sound speeds from the two test cases previously published are shown here, derived from observational data. Case A ending at 11 a.m. (black) and case B ending at 8 a.m. (green) both on November 7, 2006. Also shown is Case C (red) ending at 8 a.m. on November 8, 2006. The top image is for the entire 300 m height of the model input profile and the bottom is zoomed in for the lowest 50 m of the profile. Note that the lower portions (below ~50-60 m) of the profiles were derived by extrapolating best fit Monin-Obukov similarity profiles to SODAR-RASS data which begins at around 50 m AGL, and the lowest ~ 10 m was obtained by fitting logarithmic profiles to Sonic Anemometer data.

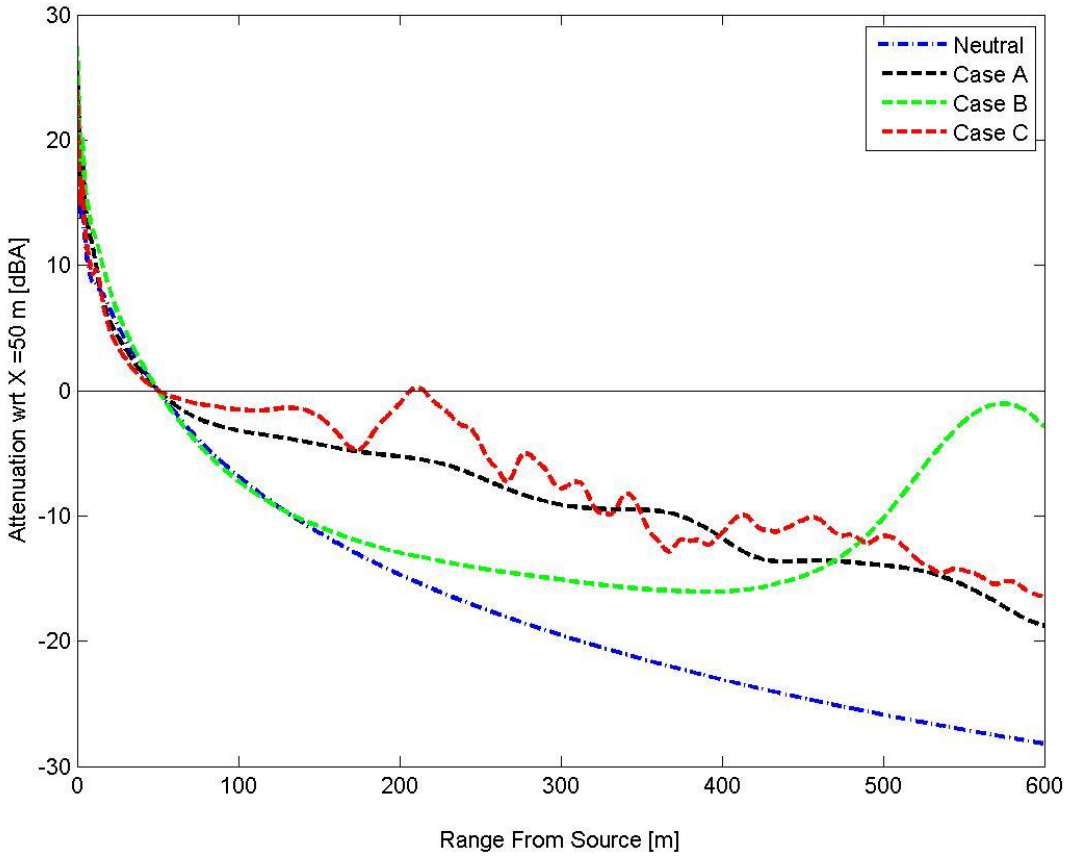

Figure C.2. Attenuation Comparisons from Ovenden et al. (2009).

From Ovenden et al. (2009), the three attenuation cases presented in that publication. Here the range plots have all been shifted based upon their respective neutral curves before computing the attenuation with respect to 50 m range.

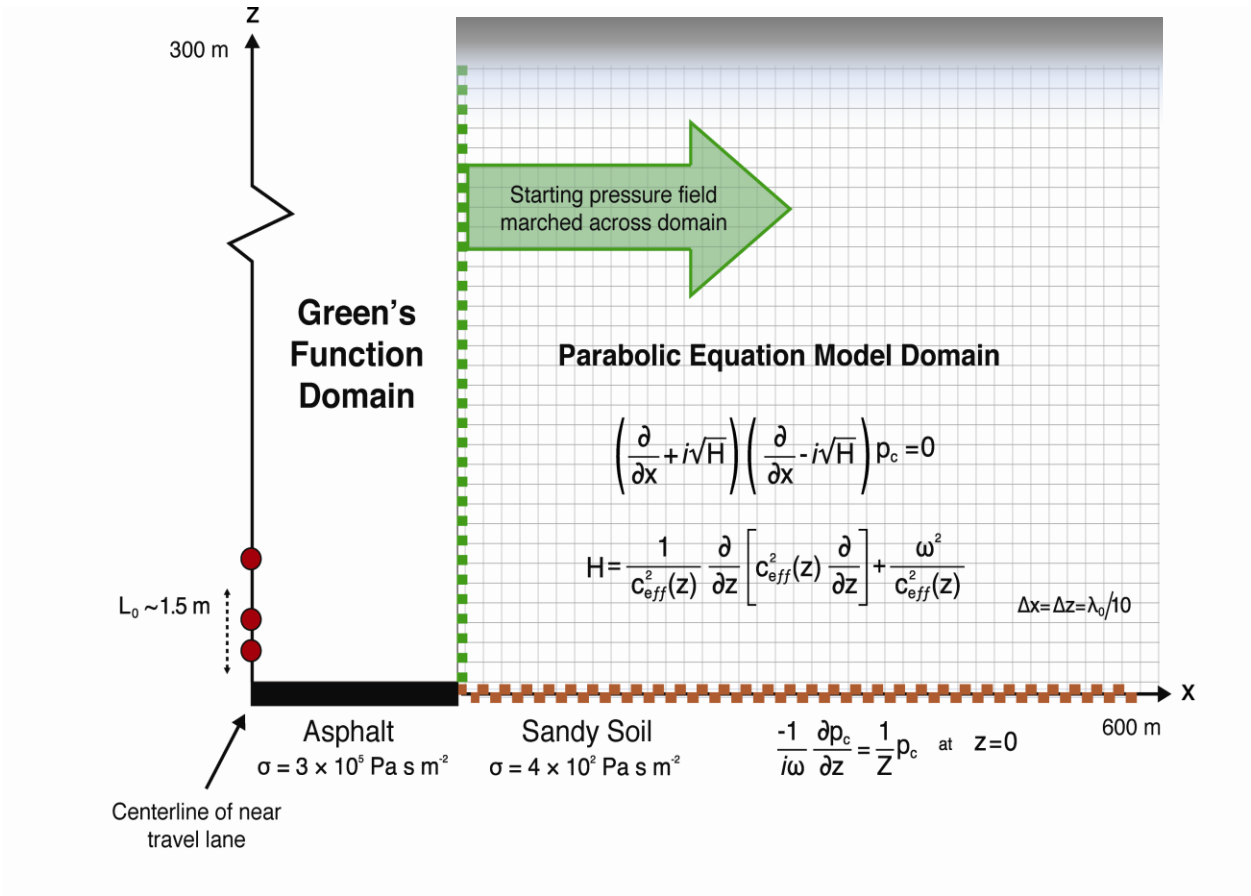

Figure C.3. PE Model Schematic Adapted from Ovenden et al. (2009).

APPENDIX D. ADDITIONAL DATA FOR GTPE GAUSSIAN TERRAIN CASE

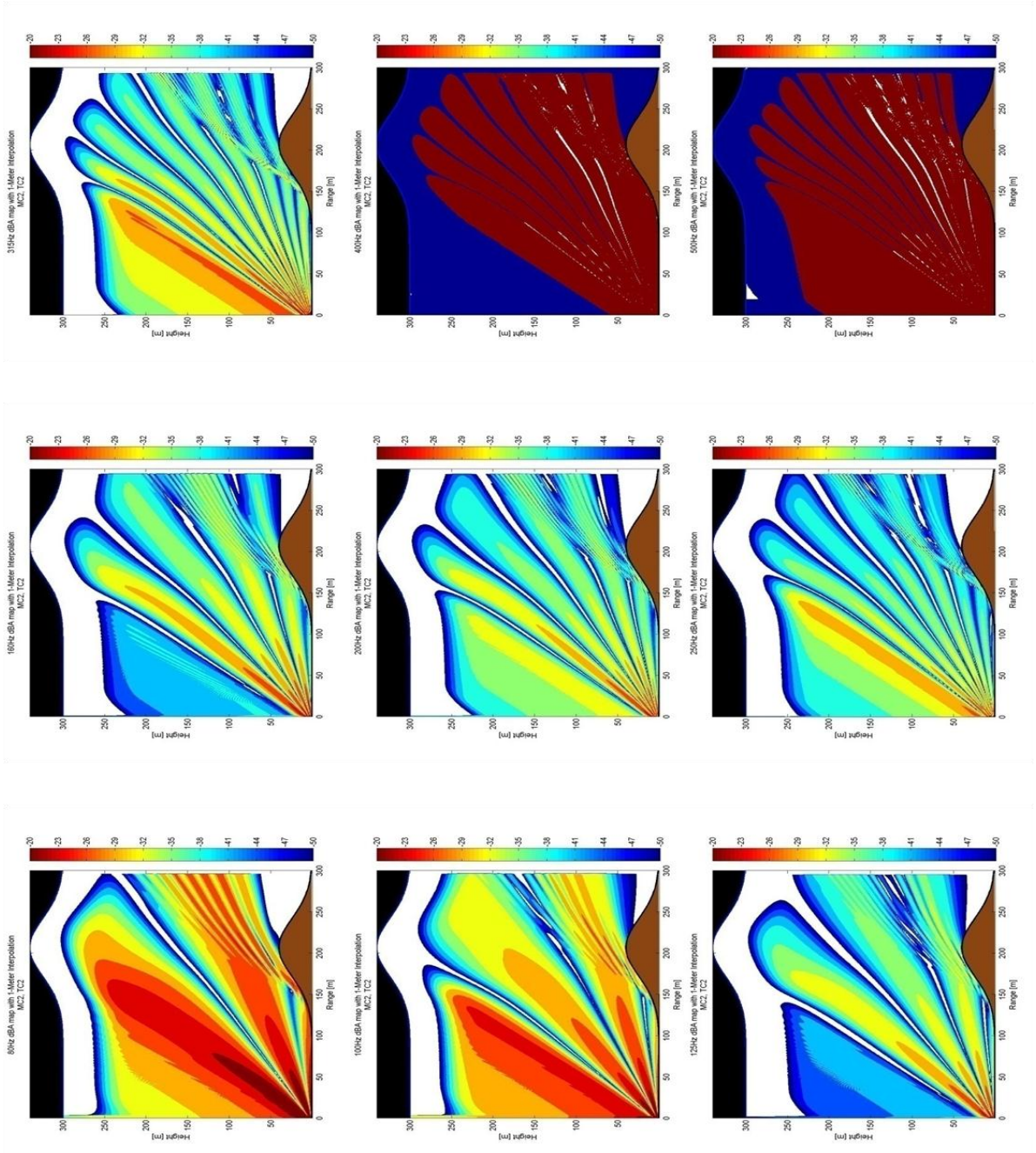

Figure D.1. Comparison of GTPE Output for Different Frequency Bands.

The contour-filling patch algorithm failed for the last two figures. Shown are frequencies arranged in 1/3 octave columns with frequency roughly doubling from one column to the next; this divides the wavelength by two and changes the interference lobes accordingly. A scaling of the domain based upon wavelength could be used, but is useful only for neutral cases.